Advanced Functional Materials

ADVANCED FUNCTIONAL MATERIALS
www.afm-journal.de

RESEARCH ARTICLE OPEN ACCESS

3D Bioprinted Glioblastoma Multiforme Models: How the Extracellular Matrix Glycosignature Influences Drug Response

Francesca Cadamuro[1] | Marco Piazzoni[1] | Ilaria Borghi[1] | Alberto Baeri[2] | Alessandro Fumagalli[2] | Federica Perillo[3] | Hafiz Muhammad Fahad[4] | Martina Ghizzi[1] | Luca Crippa[1] | Gabriella Nicolini[1] | Angela Bentivegna[1,5] | Daniele Ramazzotti[1,5] | Valentina Zuliani[6] | Mirko Rivara[6] | Carlo Giorgio Giussani[1,5] | Andrea Di Cristofori[1,5] | Guido Cavaletti[1] | Federica Facciotti[2] | Sobhan Sheikhi[7] | Claire Seydoux[8] | Murielle Salome[8] | Peter Cloetens[8] | Alberto Bravin[7,9,10] | Paola Coan[4,11] | Francesco Nicotra[1] | Laura Russo[1,5,12]

[1]School of Medicine and Surgery, Università degli Studi Milano-Bicocca, Vedano al Lambro (MB), Italy | [2]Department of Biotechnology and Biosciences, University of Milano-Bicocca, Milan, Italy | [3]Department of Experimental Oncology, European Institute of Oncology IRCCS, Milan, Italy | [4]Department of Experimental Physics – Medical Physics, Ludwig Maximilians University, Munich, Germany | [5]Fondazione IRCCS San Gerardo dei Tintori, Monza (MB), Italy | [6]Food and Drug Department, University of Parma, Parma, Italy | [7]Department of Physics, University of Milano-Bicocca, Milan, Italy | [8]European Synchrotron Radiation Facility (ESRF), Grenoble, France | [9]Department of Physics, University of Calabria, Rende, Italy | [10]INFN Sezione di Milano-Bicocca, Milan, Italy | [11]Department of Radiology, Luidwig Maximilians University, Mucich, Germany | [12]CÚRAM Research Ireland Centre for Medical Devices, University of Galway, Galway, Ireland

Correspondence: Francesca Cadamuro (francesca.cadamuro@unimib.it) | Laura Russo (laura.russo@unimib.it)

Received: 30 June 2026 | **Revised:** 30 June 2026 | **Accepted:** 7 August 2026

Keywords: 3D Bioprinting | ECM mimics | GBM models | glycosignature | hydrogels

ABSTRACT

Aberrant glycosylation is widely recognized as a hallmark of different types of cancer, including Glioblastoma multiforme (GBM). Deregulation of specific glycans' expression within the extracellular matrix (ECM) contributes indeed to the generation of the tumoral niche, playing a crucial role in disease progression, recurrence, and drug response. An in silico prioritization filter based on available GBM transcriptomic data allowed to identify ECM glycosignature that correlates with poor prognosis, thus guiding the rational design of a GBM 3D in vitro model. Following these instructions, a bioink composed of gelatin functionalized with α-NeuNAc-(2→3)-β-D-Gal- and chondroitin sulfate was synthesized, and the ECM glycosignature effect on cancer cells drug response was investigated. Multiplex immunofluorescence analysis, combined with high-resolution nano-computed tomography (nanoCT), demonstrated that specific matrix glycosignatures trigger an alternative Galectin-3 /Mucin-1 (MUC1)/Mucin-4 (MUC4) axis coupled with structural ECM remodeling to evade pharmacological cytotoxicity. The findings from this study offer valuable insights into the complex interplay between the ECM glycan cues and the drug response in GBM, paving the way to develop more predictive in vitro models for preclinical drug screening and to design glycan-targeted therapeutic strategies.

1 | Introduction

Glioblastoma multiforme (GBM), the most aggressive primary brain tumor, remains a formidable clinical challenge due to its highly infiltrative nature, intratumoral and intertumoral heterogeneity, and resistance to conventional therapies [1, 2]. The complex tumor microenvironment (TME) plays a crucial role in GBM progression, drug response and recurrence. Indeed, the cross-talk between the tumor and the surrounding tissue helps cells to survive and escape treatments [3]. Immunotherapies,

which have been successfully developed for other tumors, have shown limited efficacy in GBM [4]. To date, the standard treatment for newly diagnosed GBM is surgical resection followed by radiotherapy with concurrent and adjuvant chemotherapy with temozolomide (the STUPP protocol) [5]. However, the average overall survival remains around 12–18 months [6].

Aberrant glycosylation plays an important role in promoting tumor growth and immune suppression; however, the human glycome in GBM is still largely unexplored [7]. It has been suggested that the deregulation of glycosylation-related gene expression contributes to GBM heterogeneity and has significant predictive value for patient survival [8]. It is now well established that sialic acids and glycosaminoglycans (GAGs) contribute to tumor growth and invasion by modulating cell signaling and promoting extracellular matrix (ECM) remodeling [9–13]. Indeed, α-2,3- linked sialic acid (NeuNAc) on galactose (Gal) or N-acetylgalactosamine (GalNAc) residues plays an important role in immune evasion. These sialylated motifs act as ligands for inhibitory receptors (i.e., Siglecs) on immune cells, thereby suppressing immune activation [14–16].

Therefore, the development of new tissue models mimicking not only the protein composition and the stiffness of GBM TME, but also its glycosignature, is essential for the development of more effective therapies.

Conventional two-dimensional (2D) models inadequately capture the complexity of the native TME, limiting their translational relevance for animal-free drug testing based on human pathological tissue models [17–19]. To overcome these limitations, three-dimensional (3D) bioprinting has emerged as a powerful tool for engineering in vitro tumor models that more accurately mimic the structural and functional complexity of GBM [20–22]. Recent advancements in 3D bioprinting have focused on the development of multicomponent constructs to better recapitulate the heterogeneous nature of the TME and on precisely controlling the physical-mechanical properties to influence cell behavior and signaling pathways [23–25]. Furthermore, significant efforts have been directed toward incorporating specific biomolecules to enhance the biomimicry of these in vitro models [26, 27]. Among them, the use of glycans, which are heavily involved in cell fate modulation and tumor behavior, remains largely unexplored [19, 28, 29].

There is a need for efficient approaches to define the correct glycosignature to develop tailored GBM tissue models containing patient-derived cells and to inform personalized drug treatments. In this work, we engineered a 3D bioprinted hydrogel incorporating patient-derived GBM cells and rationally selected a glycosignature to faithfully mimic the tumor microenvironment, enabling the assessment of how matrix composition influences cell fate and drug resistance. By combining multiplex immunofluorescence analysis and high-resolution nanocomputed tomography (nanoCT), we identify glycan-mediated ECM remodeling as a key modulator of the TME and the drug response.

2 | Results and Discussion

2.1 | Development of 3D Bioprinted Hydrogel Constructs

To evaluate in depth how specific glycosignatures within the GBM TME affect drug response, we developed an in vitro 3D bioprinted GBM model. We incorporated two glycans upregulated in GBM as reported in the literature and databank: chondroitin sulfate (CS) and α-NeuNAc-(2→3)-β-D-Gal- motifs (3'SialGal). These glycans are known to regulate key cellular processes, including matrix adhesion, growth factor signaling, tumor invasion, and therapeutic penetration [9, 30, 12, 31].

We developed four 3D bioprinted hydrogels constructs composed of hyaluronic acid (HA) and gelatin (GEL): a first without glycans (**HA-GEL**), a second functionalized with α-NeuNAc-(2→3)-β-D-Gal- (**HA-GEL-3'SialGal**), a third containing CS (**HA-GEL-CS**), and a fourth containing both α-NeuNAc-(2→3)-β-D-Gal- and CS (**HA-GEL-3'SialGal-CS**) (see Figure 1). To ensure cell viability during and after the printing process, while allowing precise control over the hydrogel network architecture, the polymeric components, HA, GEL, and CS, were functionalized with a linker containing an azido group to perform the cross-linking via strain-promoted azide-alkyne cycloaddition (SPAAC) with 4arm-PEG-DBCO. SPAAC is a catalyst-free, bioorthogonal reaction that proceeds rapidly under physiological conditions without generating cytotoxic by-products [32, 33], making it highly suitable for 3D bioprinting applications.

The α-NeuNAc-(2→3)-β-D-Gal- unit was attached to gelatin by reductive amination with $NaBH_3CN$ of the "reducing end" of α-NeuNAc-(2→3)-β-D-Gal-(1→4)-D-Glc with the lysine residues of gelatin. In this way the D-glucose unit of α-NeuNAc-(2→3)-β-D-Gal-(1→4)-D-Glc acts as a linker to join α-NeuNAc-(2→3)-β-D-Gal- to gelatin (see Figure 1).

HA was condensed with an N_3-PEG-NH_2 linker via DMTMM, generating HAN_3 as previously reported [15]. Gelatin was condensed with N_3-PEG_4-COOH via EDC/NHS, generating $GELN_3$ [15]. CS was condensed with an N_3-PEG-NH_2 linker, adapting the procedure reported by Hu et al. [16], and the conjugated polymer CSN_3 was characterized by ^{1}H NMR and FTIR analysis in comparison with the unfunctionalized one (CS) (Figure S1). CS has a 4-sulfate to 6-sulfate ratio 4S/6S = 2.55 [13]. The ^{1}H NMR spectrum (Figure S1A) of azide-functionalized chondroitin sulfate (CSN_3) shows characteristic signals corresponding to both the modified polysaccharide backbone and the attached azide-terminated PEG chain. A distinctive signal at 3.4 ppm corresponds to $-CH_2N_3$, and an increased signal intensity around 3.6 ppm is observed, consistent with the presence of the 14 methylene protons of the PEG spacer (six $-CH_2-O-$ units and one $-CH_2-N-$ group). The degree of functionalization, determined by integration of the peak at 2.04 ppm due to the $-CH_3$ of the acetamide of CS and the increase in the peaks at 3.6 ppm, resulted 22% (w/w). The ^{13}C NMR is reported as supplementary information (Figure S2). The FT-IR spectrum of CSN_3 (Figure S1B) confirms the successful functionalization by the characteristic azide absorption band at ~2100 cm^{-1} which is indicative of the presence of N_3 groups (Supporting Information).

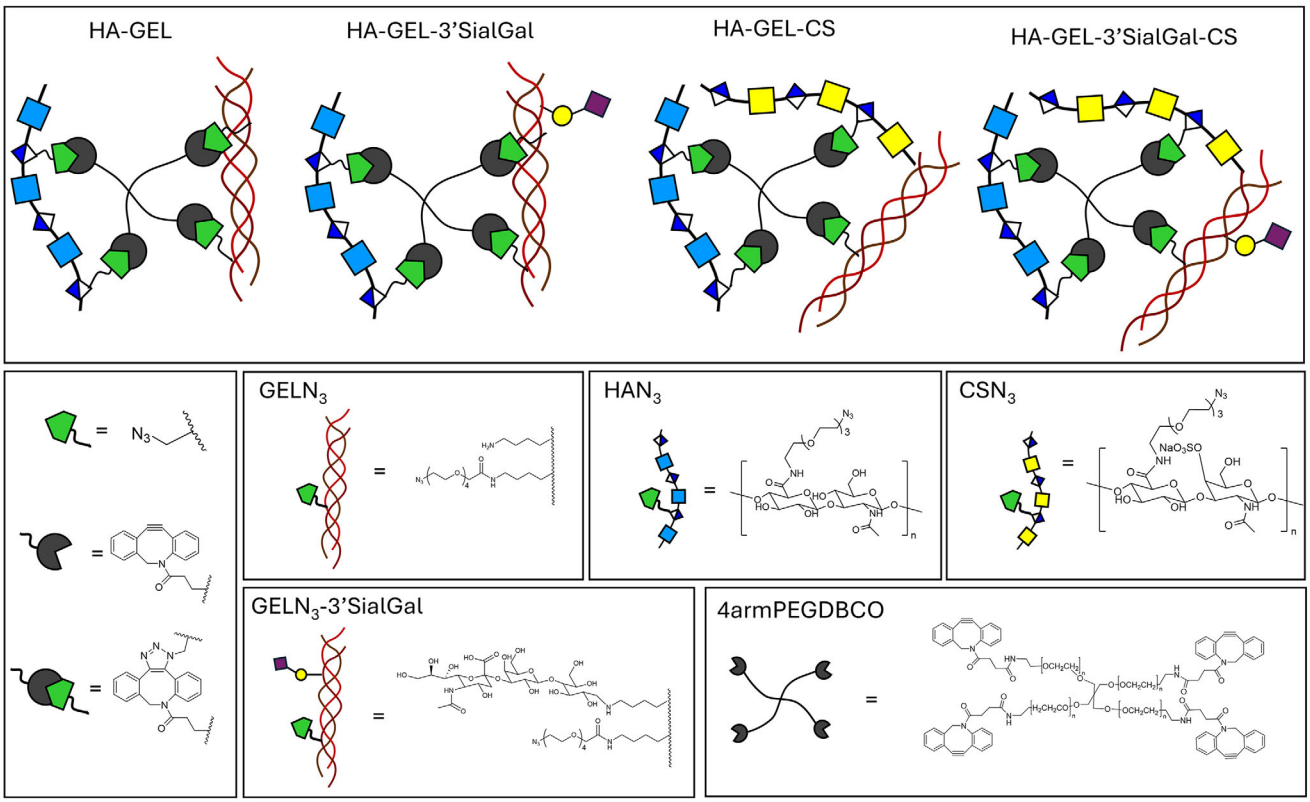

FIGURE 1 | Illustration of the hydrogel structures: HA-GEL, HA-GEL-3'SialGal, HA-GEL-CS, and HA-GEL-3'SialGal-CS.

The cross-linking of azide-functionalized biopolymers was achieved using a four-arm polyethylene glycol functionalized with dibenzocyclooctyne (DBCO) groups (4arm-PEG-DBCO). Compared to linear PEG analogues, the multi-arm architecture of 4-arm-PEG-DBCO provides multiple reactive sites per molecule, promoting rapid formation of a highly interconnected hydrogel network [34]. The four distinct hydrogel formulations HA-GEL, HA-GEL-3'SialGal, HA-GEL-CS, and HA-GEL-3'SialGal-CS were obtained by combining the proper components and performing the cross-linking reaction with 4arm-PEG-DBCO.

The four hydrogels display minimal variations in their structural and mechanical properties as demonstrated by SEM imaging (Figure 2A), swelling behavior (Figure 2B) and rheological amplitude sweep analysis. (Figure 2C,D). SEM analysis revealed that HA-GEL possesses a compact matrix with sparsely distributed, irregular pores, which correlates with its relatively lower swelling capacity. In contrast, the incorporation of α-NeuNAc-(2→3)-β-D-Gal- in HA-GEL-3'SialGal results in a more fragmented and sponge-like network. This structural change can be attributed to the presence of hydrophilic sialic acid residues, which enhance water absorption. HA-GEL-CS displays a more organized and interconnected porous structure, which facilitates moderate swelling. Notably, the combination of both CS and α-NeuNAc-(2→3)-β-D-Gal- in HA-GEL-3'SialGal-CS leads to a higher number of pores and more uniform in size compared to the other hydrogels, resulting in a more ordered porous network structure and ultimately contributing to the highest swelling capacity observed. The negatively charged sulfate groups in CS promote electrostatic repulsion and water uptake at physiological pH, enhancing swelling in both CS-containing hydrogels. Additionally, the presence of sialic acid residues in HA-GEL-3'SialGal-CS further increases hydration and porosity, likely due to cooperative interactions between sulfate and sialic acid moieties that enhance the hydrogel's capacity to retain water.

Rheological amplitude sweep analysis confirmed typical gel-like behavior for all samples, with storage modulus (G') exceeding loss modulus (G″) in the linear viscoelastic region (LVR). HA-GEL-3'SialGal showed the highest G' (G' = 320 ± 30 Pa), reflecting moderate improvements in stiffness and mechanical stability, followed by HA-GEL (G' = 270 ± 30). Conversely, CS-containing formulations (HA-GEL-CS and HA-GEL-3'SialGal-CS) exhibited slightly lower G' values (respectively, G' = 220 ± 10 and G' = 240 ± 20) and delayed crossover points, reflecting a more flexible and compliant network, where polymer chains can undergo greater deformation before structural breakdown (Figure 2D). Overall, while the four formulations exhibit comparable viscoelastic features, porosityand swelling capacity, HA-GEL-3'SialGal-CS stands out as the most effective at mimicking the native matrix architecture and stiffness of the GBM microenvironment [35, 36].

The preliminary biological evaluation of 3D bioprinted models was conducted using the commercial U87 GBM cell line. Cell viability and spatial organization inside the 3D bioprinted models were evaluated after 14 days of cell culture. To ensure homogeneous distribution of tumor cells while maintaining a construct geometry suitable for handling, imaging, and sectioning, a droplet-based 3D printed process was exploited (Figure 2E,F and Figure S3). Notably, this specific configuration allows uniform cell seeding and facilitates subsequent sectioning for histological and molecular analysis [37, 38].

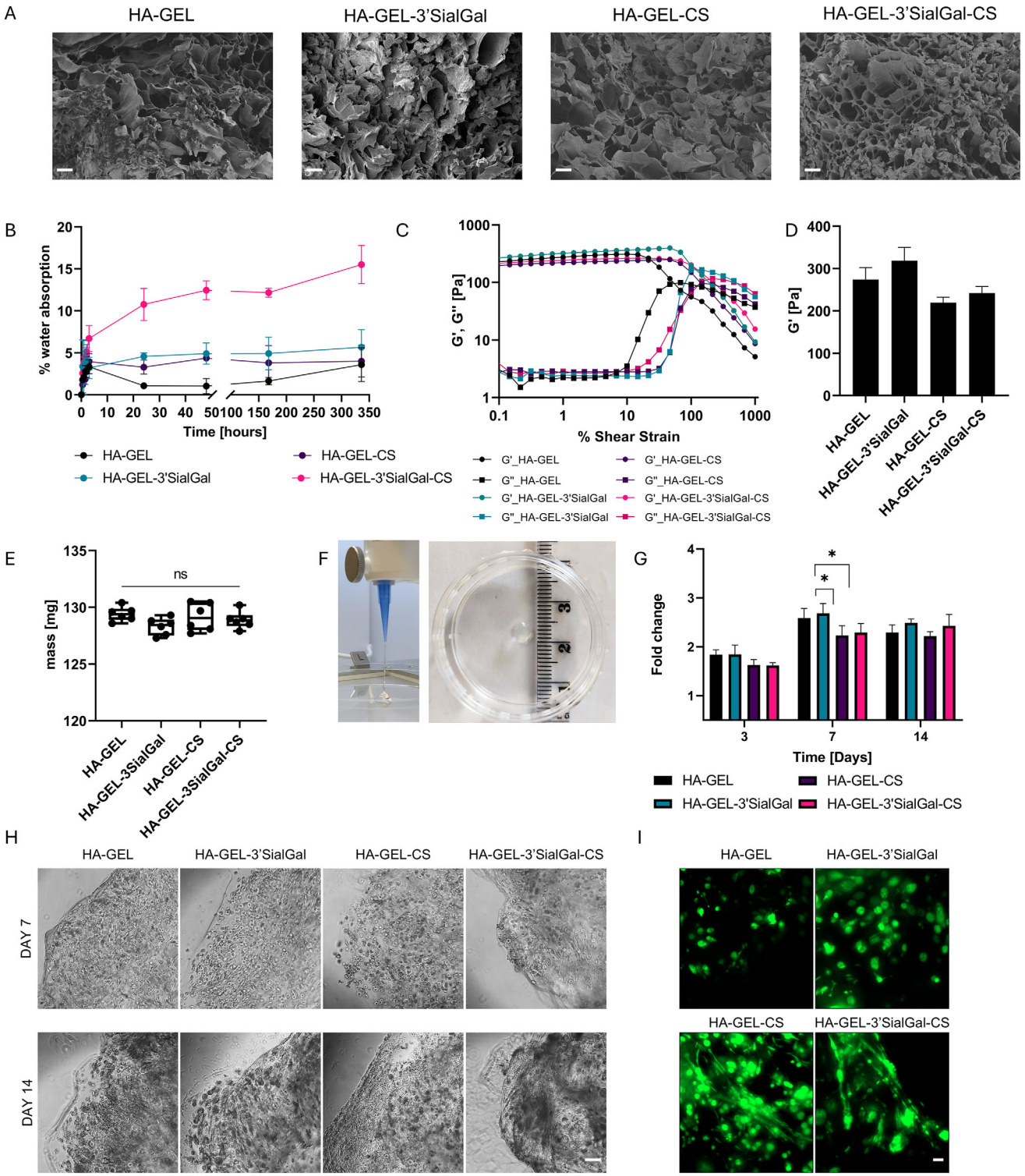

FIGURE 2 | Physico-mechanical and biological characterization of hydrogels. (A) SEM images respectively of HA-GEL, HA-GEL-3'SialGal, HA-GEL-CS, and HA-GEL-3'SialGal-CS; scale bar 100 μM. (B) Swelling test, (C, D) Amplitude sweep analysis, (E) weight of 10 printed drops for each formulation, showing high reproducibility and no statistically significant differences among formulations. Data ($n = 10$) are presented as box plots (median, 25th–75th percentiles; whiskers indicate minimum and maximum values). (F) Representative images of the flow test and a 3D-printed drop, (G) Alamar blue assay, (H) BF images of U87 cultured in 3D bioprinted hydrogels. Scale bar 50 μM. (I) LIVE/DEAD fluorescence images of U87 cultured in 3D bioprinted hydrogels for 14 days. Green fluorescent signal indicates alive cells. Scale bar 50 μM. Data ($n = 3$) are presented as mean ± SD. ns = non-significant, $^*p > 0.05$.

Bright-field imaging (Figure 2H) shows that some modest differences started to appear between the conditions over time. In HA-GEL-CS and HA-GEL-3'SialGal-CS, cells progressively elongated and aggregated into multicellular networks, suggesting an active process of morphogenesis. In contrast, HA-GEL hydrogels supported limited aggregation, with cells predominantly forming spheroidal clusters. Overall, the inclusion of CS, particularly in HA-GEL-3'SialGal-CS, promotes cell spreading, aggregation, and the formation of more complex, tumor-like structures within the hydrogel matrix, consistent with previous findings reported in the literature [36, 39–41].

LIVE/DEAD assays (Figure 2I) confirm a high proportion of viable cells across all conditions, indicating that the bioprinting process preserved cell integrity and was compatible with long-term culture. Notably, differences in cell distribution and morphology were observed among the formulations. The presence of CS and sialylated glycosignatures promotes enhanced cell–cell interactions, proliferation, and supports the formation of tumor-like niches, potentially influencing GBM cell behavior and drug responsiveness [41–43]. Alamar Blue assay (Figure 2G) confirmed good viability in all formulations. In the first 7 days, formulations without CS resulted in more metabolically active cells than those containing CS, probably due to the onset of differentiation in the CS-containing hydrogels, as observed in the LIVE/DEAD fluorescence images after 14 days.

Since the material was not cytotoxic, we proceeded with a preliminary investigation of biomarker expression via immunofluorescence (IF) analysis. To enhance the biological relevance of the 3D bioprinted GBM model, the initial study, conducted using U87 cells, was expanded to include patient-derived G166 GBM stem cells. While U87 cell lines are widely used as a baseline for resistance due to their robust in vitro handling and reproducibility, they fail to recapitulate the genetic heterogeneity and the resistance to therapeutic pathways that are characteristic of human GBM. G166 preserves the primary molecular signature of GBM, with a phenotype that includes clinically relevant features, like the retention of glioma stemness, the differentiation potential, and a high invasive nature associated with ECM remodeling. Both cell lines were encapsulated in the HA-GEL-3'SialGal-CS hydrogel formulation, which had previously demonstrated a strong ability to support tumor-like features. Preliminary IF results revealed that U87 cells were inadequate to recapitulate key GBM biomarkers, G166 (Figure S4). Images validated this rationale showing that U87 cells predominantly formed more uniform spheroids with lower expression of key pathophysiological markers. On the contrary, G166 within the glycosylated matrix successfully recapitulated specifically: upregulation of core stemness (CD44, Nestin), proliferation (Ki67), and key regulatory factors involved in drug resistance (ALKBH5, ALKBH2). Consequently, the subsequent investigations were carried out using the G166.

2.2 | In Silico Prioritization of GBM-Relevant Glycosignature-Associated Markers

To support the rational selection of glycosignature-associated components and phenotypic markers, we performed an exploratory in silico analysis of selected genes related to HA and CS metabolism, sialylation, ECM remodeling, stemness, proliferation, hypoxia, invasion, and drug-resistance-associated processes (Table S1). Gene expression distributions were assessed in publicly available GBM datasets, PanCancerAtlas and Clinical Proteomic Tumor Analysis Consortium (CPTAC). This analysis was used as a prioritization layer to guide the selection of biologically relevant glyco-ECM axes and marker panels for downstream experimental validation in 3D bioprinted GBM models. A multivariate Cox proportional hazards regression model was generated, including patient age and gender as clinical covariates. Initially, a comprehensive screening was performed on an extended panel of microenvironment- and glycosylation-related genes (Table S2). However, evaluating this large panel introduced high multicollinearity among co-expressed pathway components. This redundant statistical signaling affected the model, causing most variables in Table S2 to show flat hazard ratios and non-significant p-values.

To overcome this statistical limitation and extract meaningful biological insights, the multivariate analysis was restricted to a refined, biology-driven panel of 71 prioritized genes (Tables S1 and S3). Within this targeted model, distinct and highly significant survival associations clearly emerged. Specifically, the in silico screening highlighted a significant dysregulation within the sialylation patterns of the *ST3GAL* family (encoding the -2,3-sialyltransferases) and the CS sulphation pathway, highlighted by the high statistical significance of the 4-sulfotransferase *CHST11*. Furthermore, alterations were observed in other carbohydrate-binding markers such as *LGALS1* and *LGALS3*, as well as oncogenic mucins like *MUC1* and *MUC4*. The screening also highlighted the fucosyltransferase FUT4, which is responsible for the synthesis of the stage-specific embryonic antigen-1 (SSEA-1 or Sialyl-SSEA-1). The modelling also confirmed a highly significant survival association for critical phenotypic drivers, including *MKI67 encoding for the proliferation marker Ki-67*, the neural progenitor marker *NES* (Nestin), the transcription factor *FOXM1*, and the demethylases *ALKBH2* and *ALKBH5*.

Collectively, these in silico findings are not employed as prognostic quantification, but to support the design of a glycoengineered matrix providing a rationale for the inclusion of α-NeuNAc-(2→3)-β-D-Gal-and chondroitin sulfate (CS) within the HA-GEL bioink architecture.

Based on these in silico results, which highlighted specific dysregulations within the metabolic and structural axes of the TME, we selected a comprehensive immunofluorescence (IF) panel, prioritizing the direct phenotypic transducers of transcriptional alterations as candidate biomarkers for in vitro drug screening. Within this framework, alterations in HA metabolism and matrix pathways guided the selection of CD44 and Fibronectin to track matrix interactions, while dysregulations in sialylation and sulfation dictated the inclusion of Galectin-3, MUC1, and MUC4 to monitor anti-apoptotic drug-escape mechanisms. To track the adaptive response and resistance networks, we targeted CHI3L1, FOXM1, Survivin, and the hypoxic driver HIF-1α, further evaluating tumor hierarchy and growth through the stemness and proliferation markers CD133, CD15, Ki-67, and p53. Finally, the panel was completed with the epigenetic regulators ALKBH5 and ALKBH2 as indicators of phenotypic plasticity in response

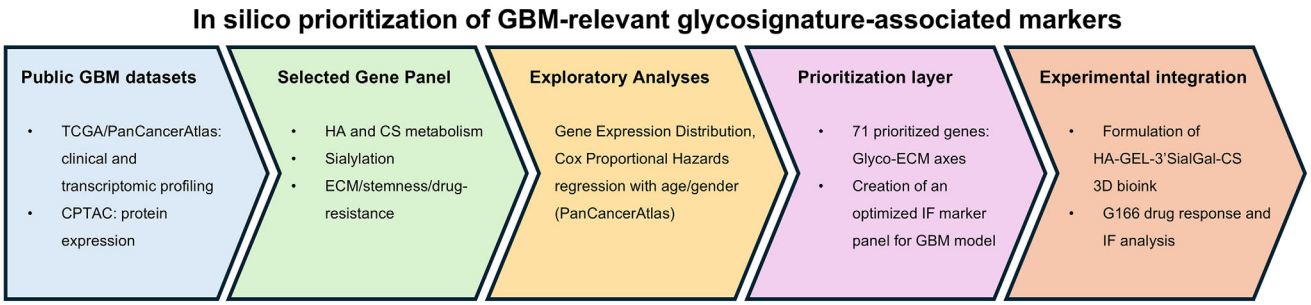

FIGURE 3 | In silico prioritization workflow used to support the selection of GBM-relevant glyco-ECM axes and immunophenotypic markers. Public GBM transcriptomic and clinical datasets were used to evaluate expression distributions (violin plot) (Figures S5 and S6) of a curated glycosignature- and GBM-associated gene panel and to explore survival associations using Cox proportional hazards models with clinical covariates. The analysis guided the selection of glyco-ECM cues and marker panels for downstream experimental validation in 3D bioprinted GBM models.

to MV1035 treatment. This approach allows us to observe how patient-derived resistance networks are modulated by our specific glycosignatures, effectively validating the 3D bioprinted model as a robust platform for pharmacological testing (Figure 3).

2.3 | Multiplex Immunofluorescence Identifies ECM Glycosignature Effects on Drug Response

Drug testing to evaluate treatment efficacy and resistance mechanisms was performed on the four 3D bioprinted constructs (HA-GEL, HA-GEL-3'SialGal, HA-GEL-CS, and HA-GEL-3'SialGal-CS) seeded with G166 using (a) temozolomide (TMZ), (b) MV1035, an inhibitor of ALKBH2 and ALKBH5, reported to overcome TMZ resistance in GBM stem cell lines [44], (c) a combination of both agents (TMZ_MV1035), and (d) a DMSO control included at the highest concentration applied across treatments. The results demonstrated that, depending on the ECM-mimic composition, distinct drug-specific resistance pathways were activated in G166. In detail, treatments were initiated 7 days post-printing to allow high cell density and organization in spheroids. This specific timeline has been selected to ensure the full adaptation of encapsulated cells to the structural and biochemical cues of the hydrogels.

Representative brightfield images (Figure S7) revealed initial variations in cell morphology and aggregate distribution across different hydrogel formulations and treatment conditions. In particular, G166 clusters embedded in the fully glycosylated HA-GEL-3'SialGal-CS and treated with MV1035 and the combination TMZ_MV1035 appeared smaller with respect to the non-treated control.

A multiplex IF analysis was performed to evaluate and demonstrate that the glycosignatures induce distinct phenotypes in G166 during different and combined therapeutic treatments (Figure 4). The multiplex IF data confirmed that the glycosignature derived by the selected proteins and enzymes in the ECM is involved in the activation of specific resistance phenomena. In untreated conditions (Figure 4A), G166 maintains a predominantly quiescent state across all the glycosignatures tested, with low expression of the proliferation marker Ki-67 and stemness factors like CD133, Nestin, and ALKBH5. These data suggest that G166 could adapt to the glycosylated matrix, recreating a protective and non-proliferative stem cell niche that is typical of the native GBM microenvironment.

In vivo, the interaction between HA receptors like CD44 and sulfated GAGs is known to anchor G166 in a specialized extracellular niche, maintaining the cells in a state that shields them from spontaneous differentiation [45–48]. After treatment, the CS component emerges as the primary driver of cell plasticity and alternative resistance. Notably, with TMZ treatment (Figure 4C), in HA-GEL-CS and HA-GEL-3'SialGal matrices, the expression of CHI3L1 was upregulated compared to HA-GEL in the non-treated condition. This is consistent with the activation of an adaptive pathway linked to GBM chemotherapy resistance, further suggesting a poor clinical prognosis analogous to that observed with the ST3GAL1/4 axis [49–51]. In contrast, CHI3L1 induction was not significantly observed in HA-GEL-3'SialGal-CS matrices, instead displaying increased Galectin-3, MUC1, and, to a lesser extent, MUC4 expression, indicating the engagement of alternative glycan-dependent survival mechanisms. Indeed, high Galectin-3 expression has been reported to protect GBM cells from temozolomide-induced cytotoxicity [52, 53]. This is supported by the possible interaction between Galectin-3 with heavily glycosylated mucins such as MUC1 and MUC4, also upregulated in HA-GEL-3'SialGal-CS, supporting a glycan-dependent adaptive response to chemotherapy [54–56].

Upon MV1035 administration (Figure 4E), in the CS-rich hydrogel matrix (HA-GEL-CS and HA-GEL-3'SialGal-CS), a reduction in the stemness marker CD133 occurs, with a concomitant upregulation of ALKBH5, suggesting a shift toward a highly plastic and proliferative state.

Combined TMZ and MV1035 treatment (Figure 4G) induced a robust and matrix-dependent stress response across all hydrogel formulations, prominently characterized by a marked upregulation of HIF1α compared to HA-GEL untreated controls. Although HIF1α was upregulated in all conditions, downstream responses were clearly dependent on matrix composition. In CS-containing hydrogels, FOXM1 expression was increased, with a stronger effect observed particularly in HA-GEL-CS. In contrast, FOXM1 was downregulated in HA-GEL-3'SialGal hydrogels, suggesting that sialylation alone is not sufficient to adaptive responses associated with FOXM1 under combined treatment. This suggests that chondroitin sulfation patterns may play a synergistic role with

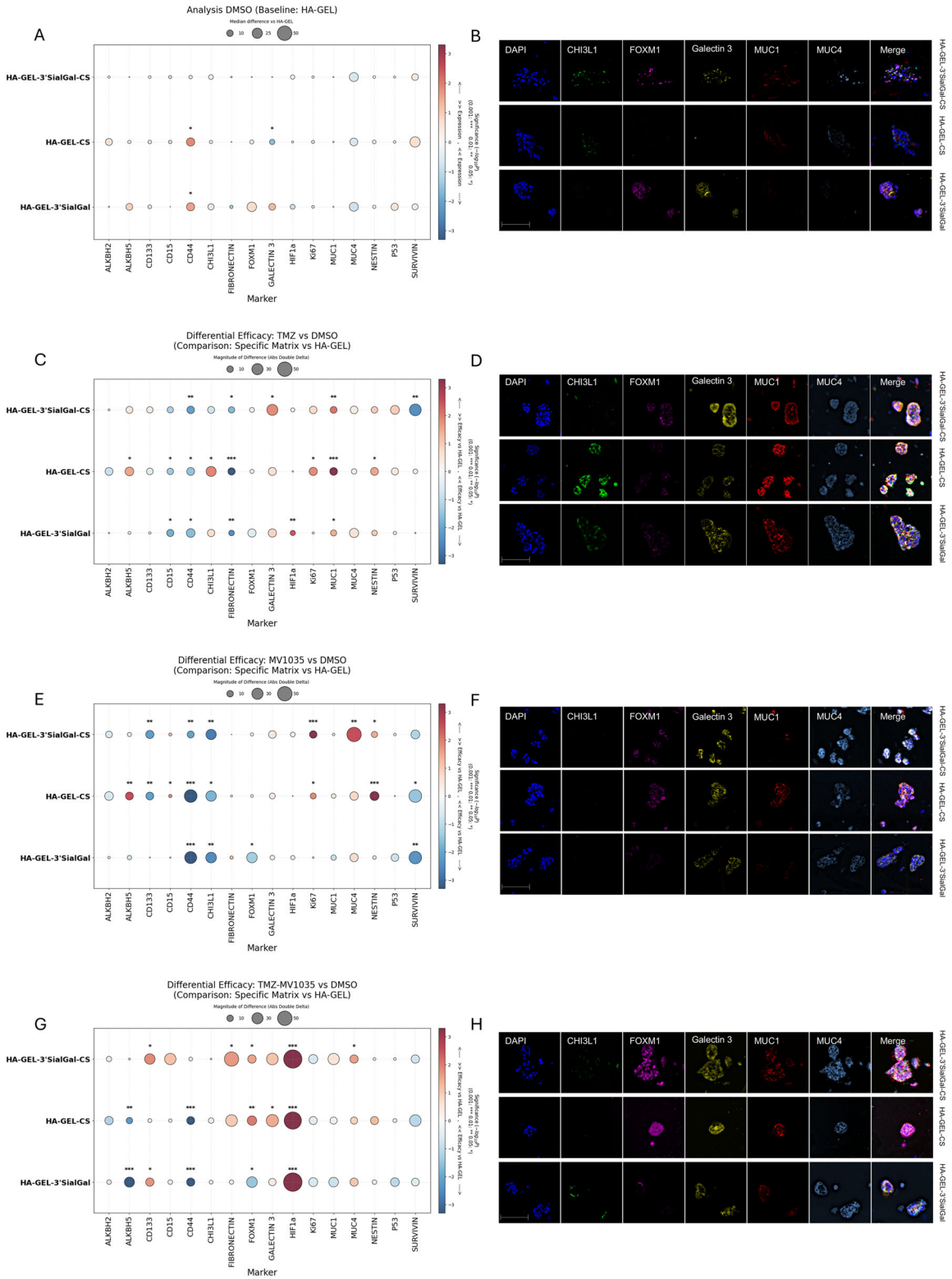

FIGURE 4 | Differential biomarker expression and multiplex immunofluorescence analysis of matrix-specific treatment responses. Bubble plots of differential expression of selected biomarkers across HA-GEL, HA-GEL-3'SialGal, and HA-GEL-3'SialGal-CS matrices under (A) DMSO baseline conditions and after treatment with (C) TMZ, (E) MV1035, or (G) TMZ_MV1035. Bubble size represents the magnitude of the effect (absolute difference or absolute double-delta values), while color intensity indicates the direction and extent of expression change relative to the HA-GEL reference condition, with red and blue denoting positive and negative changes, respectively. Statistical significance is indicated by asterisks (*$p < 0.05$, **$p < 0.01$, ***$p < 0.001$), reflecting comparisons performed against the representative qualitative multiplex immunofluorescence images corresponding to each experimental condition showing expression and spatial distribution of DAPI (nuclei), CHI3L1, FOXM1, Galectin-3, MUC1, and MUC4, along with merged images. 4B) DMSO, 4D) TMZ, 4F) MV1035 and 4H) TMZ_MV1035. Scale bars are 100 μm. Statistical interpretation integrates both the magnitude of differential expression and significance thresholds, enabling identification of biologically relevant treatment-associated changes within specific ECM contexts.

sialylated glycans in the regulation of downstream oncogenic transcription factors like FOXM1 during pharmacological stress. The most complex response and adaptive strategy was observed in the fully glycosylated HA-GEL-3'SialGal-CS matrix, mimicking the highest-risk clinical configuration. In this 3D GBM model, the synergy between α-NeuNAc-(2→3)-β-D-Gal and CS enabled a cell survival shift that bypassed the standard CHI3L1 signals, replaced by a Galectin-3/MUC1/MUC4 axis. This transition is particularly important, considering that CHI3L1 is traditionally upregulated as a generic marker of tissue duress and mesenchymal differentiation in GBM [57]. In contrast, relevant matrix glycosignatures operate through a more integrated mechanism involving Galectin-3 and mucins [58, 56, 46]. This switch suggests a glycosignature-mediated anti-apoptotic signaling, effectively shielding tumor cells from the cytotoxicity of combined treatments through an escape mechanism that is not present in the basal HA-GEL controls [54–56, 59]. In summary, these data highlight the distinct functional roles of matrix glycosignature, which result in differential survival strategies. While NeuNAc-(2→3)-D-Gal mediates the resistance to TMZ predominantly via the traditional stress-response pathway, CS selectively drives an escape related to plasticity under MV1035 therapeutic treatment. Crucially, the combination of the fully glycosylated HA-GEL-3'SialGal-CS matrix generates a synergistic and anti-apoptotic TME, suggesting the induction of alternative signaling networks that G166 can employ for drug-toxicity escape (i.e., Galectin-3/MUC1/MUC4 axis or ALKBH5 upregulation).

These experimental outputs are in line with the upstream in silico prioritization analysis (Section 2.2).

2.4 | High-Resolution nanoCT Identifies Matrix- and Treatment-Dependent Variations

To correlate the observed biomolecular adaptations with the physical evolution of the TME in the HA-GEL-3'SialGal-CS model in comparison to HA-GEL, we performed x-ray nano-computed tomography (nanoCT) analysis applying the nano-holotomography technique, which, to the best of our knowledge as never been used before to investigate 3D bioprinted cellular constructs [60–62]. This non-destructive technique allows to obtain complete volumetric imaging of the 3D bioprinted constructs with submicron precision, overcoming the sampling bias of conventional, histological, or imaging methods. We applied this method for the first time to analyze complex bioprinted systems, enhancing contrast and allowing detailed visualization of matrix distribution within the construct volume. Grayscale intensity values, corresponding to material density, indicate that the ECM is denser in the treated sample in comparison to the untreated (DMSO) sample, both in HA-GEL (Figure 5C) and HA-GEL-3'SialGal-CS (Figure 5D) [6, 63]. Indeed, pharmacological treatment with TMZ, MV1035, or a combination of both induced alterations of the 3D architecture. These samples exhibited an overall increase in ECM deposition and a localized remodeling of the ECM. These variations are directly correlated to the phenotypic plasticity (Nestin, ALKBH5) observed in multiplex analysis, suggesting cellular adaptation to the surrounding scaffold. Furthermore, while the DMSO control exhibited large, dense cell aggregates, in the samples treated with the drugs, cell clusters appeared smaller and more dispersed (Figure 5E). In conclusion, while drug treatment increases matrix deposition and reduces cluster size in both models, distinct morphological differences are exhibited. These experimental findings support the concept that the glycosignature influences the 3D spatial organization of the TME and ECM deposition, indicating that aggressive GBM phenotypes involve both physical features and glycosignature of the TME.

3 | Conclusions

In this work, we demonstrated that the ECM glycosignature acts as a key driver of chemoresistance and cellular plasticity in GBM. By integrating clinical computational screening of public GBM datasets, advanced 3D bioprinting, multiplex immunofluorescence, and synchrotron-based imaging, we functionally highlighted the specific contribution of each glycan component to drug-tumor interactions. This approach provided a prioritization rationale for integrating α-NeuNAc-(2→3)-β-D-Gal- and chondroitin sulfate (CS) cues within a hybrid HA-GEL bioink architecture, allowing us to develop four 3D models functionalized with and without these specific glycosignatures.

Notably, multiplex IF analysis revealed that treatment with TMZ, MV1035, and their combination induces fundamentally different adaptive responses dictated by the matrix composition. While α-NeuNAc-(2→3)-β-D-Gal- primarily drives resistance to TMZ by sustaining canonical stress response pathways mediated by CHI3L1, CS drives phenotypic plasticity, triggering alternative drug escape pathways under MV1035 through the upregulation of reprogramming markers such as ALKBH5 and FOXM1. Notably, the synergistic interplay between α-NeuNAc-(2→3)-β-D-Gal- and CS within our fully glycosylated model (HA-GEL-3'SialGal-CS) under combined pharmacological treatment shapes a unique adaptive response. Indeed, cells bypass traditional CHI3L1 stress signaling and instead activate an alternative Galectin-3/MUC1/MUC4 anti-apoptotic axis that shields them from cytotoxicity. This adaptive resistance is probably correlated with cell-ECM remodeling, as synchrotron-based analysis revealed an enhanced matrix deposition as a structural defense against pharmacological stress.

Such differential dynamics occur within a complex, multi-scale matrix organization mimicking the native GBM. Finally, our findings suggest that incorporating specific glycosignatures into preclinical in vitro models is a critical factor for more accurately recapitulating patient-specific resistance mechanisms. In this context, the glycan-matrix interface emerges as a key element of vulnerability that warrants further exploration. Our results suggest that disrupting these specific glycan-matrix interactions prevents the adaptation of the TME, providing a robust foundation for novel therapeutic strategies to overcome drug resistance in GBM.

4 | Experimental Section

4.1 | Materials

Hyaluronic Acid, N_3-PEG_3-NH_2, 4-(4,6-dimethoxy-1,3,5-triazin-2-yl)-4-methylmorpholinium chloride (DMTMM), MES,

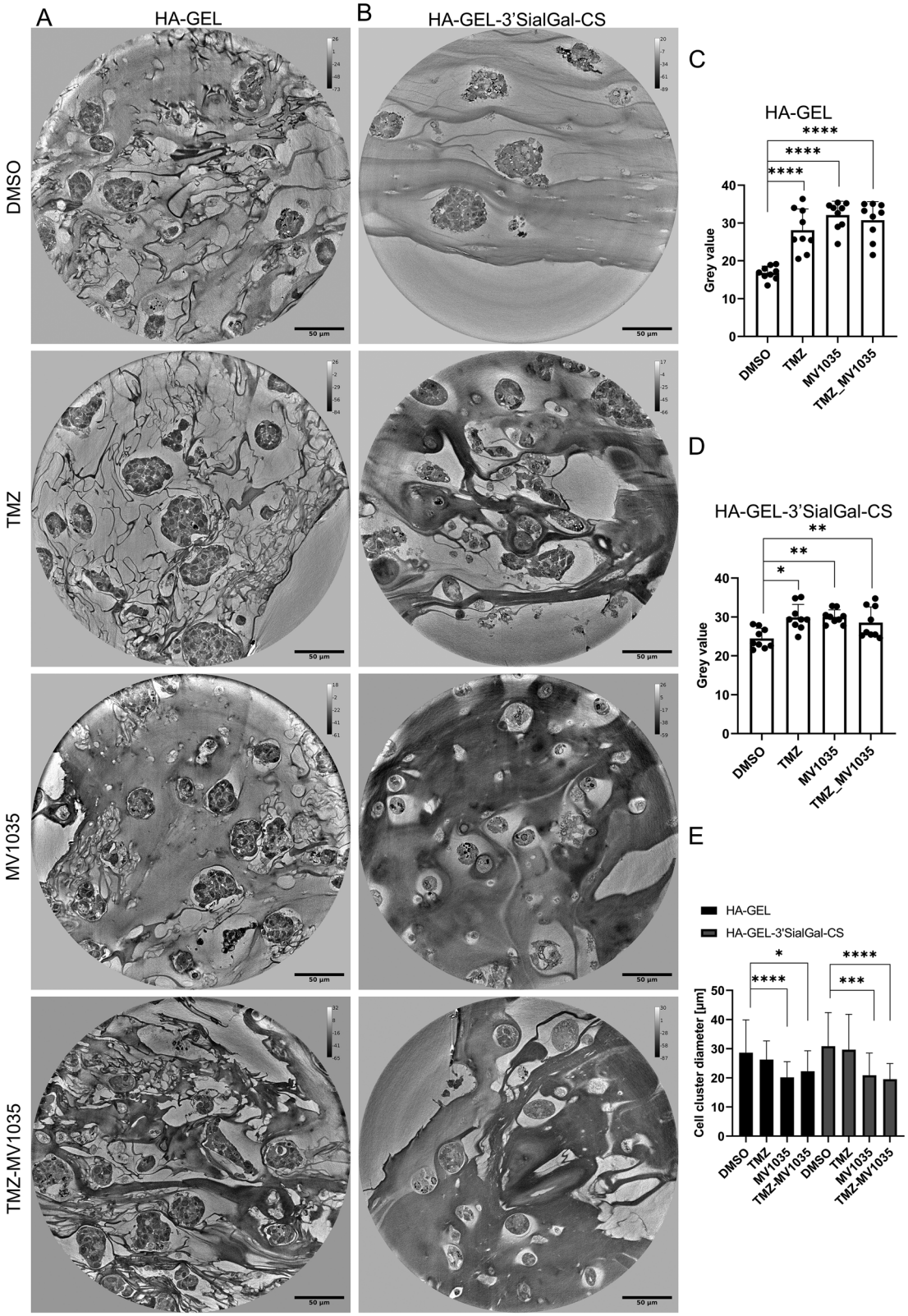

FIGURE 5 | Nano-CT structural analysis and quantitative characterization of HA-GEL and HA-GEL-3'SialGal-CS under different drug treatments. Representative high-resolution nano-computed tomography images of the full sample volume for (A) HA-GEL and (B) HA-GEL-3'SialGal-CS formulations under different treatment conditions (DMSO, TMZ, MV1035, and TMZ_MV1035. Scale bar 50 µM. (C, D) Pixel intensity average quantification respectively of HA-GEL and HA-GEL-3'SialGal-CS in each treatment condition. Data ($n = 9$) are presented as individual values. $p > 0.05$, * $p \leq 0.05$, ** $p \leq 0.01$, *** $p \leq 0.001$, **** $p \leq 0.0001$ (E) Cell cluster diameter quantifications for each ECM mimic in each condition. Data ($n = 3$) are presented as mean ± SD. $p > 0.05$, * $p \leq 0.05$, ** $p \leq 0.01$, *** $p \leq 0.001$, **** $p \leq 0.0001$.

chondroitin sulfate (MW 30000; purity >90%) were purchased from Biosynth; Phosphate Buffered Saline (PBS), N_3-PEG_4-COOH, 1-ethyl-3-(3-dimethylaminopropyl) carbodiimide (EDC) were purchased from Tokyo Chemical Industry Co.; N-hydroxysuccinimide (NHS), sodium cyanoborohydride ($NaBH_3CN$), Type A porcine skin-derived gelatin, 4arm-PEG-DBCO (Mn 20000), Fetal bovine serum, Penicillin-Streptomycin, Dulbecco's Modified Eagle Medium (DMEM), L-Glutamine, Sodium pyruvate, Live/Dead Cell Viability Assay kit obtained from EMD Millipore Corp, Bovine serum albumin (BSA), Paraformaldehyde, Triton X, were purchased from Merck. Phalloidin Alexa Fluor 647, 4',6-diamidino-2-phenylindole (DAPI) were obtained from Thermo Fisher Scientific; 3'-sialyllactose was kindly provided by Ch Hansen A/S (Hørsholm, Denmark); the U87 cell line from LGC Standards S.r.L. All reagents were purchased from Merck unless otherwise specified.

4.2 | Azide Functionalized Hyaluronic Acid (HAN_3)

Azide functionalized HA was prepared as reported in [64]. Briefly, HA (100 mg, 0.26 mmol) was dissolved in MES buffer pH 5.5 (20 mL) in a 100 mL flask for three hours. DMTMM (146 mg, 0.53 mmol) was added to the HA solution. After 40 min, N_3-PEG-NH_2 (115 mg, 0.53 mmol) was added, and the solution was stirred overnight, dialyzed with a 14 kDa cellulose membrane against NaCl 0.1 M for 2 days and then against Milli-Q water for 2 days. The obtained HAN_3 was lyophilized and stored at −20°C before use.

4.3 | Azide Functionalized Chondroitin Sulfate (CSN_3)

Chondroitin sulfate (100 mg, 0.21 mmol) was dissolved in MES buffer pH 5.5 (20 mL) in a 100 mL flask for three hours. DMTMM (115 mg, 0.42 mmol) was added to the CS solution. After 40 min, N_3-PEG-NH_2 (91 mg, 0.42 mmol) was added, and the solution was stirred overnight, dialyzed with a 1 kDa cellulose membrane against NaCl 0.1 M for 2 days and then against Milli-Q water for 2 days. The obtained CSN_3 was lyophilized and stored at −20°C before use.

4.4 | Azide Functionalized Gelatin ($GELN_3$)

Azide functionalized gelatin was prepared as reported in [64]. Briefly, N_3-PEG_4-COOH (50 mg, 0.17 mmol) was dissolved in PBS 5.5 (3 mL) in a bottom round flask at rt. Then, EDC (66 mg, 0.34 mmol) and NHS (40 mg, 0.34 mmol) were added under gentle stirring. Meanwhile, gelatin type A (250 mg, 0.5 equivalents of lysines with respect to N_3-PEG_4-COOH) was dissolved in PBS 5.5 (10 mL) in a falcon at 37°C. After 30 min, the gelatin solution was added dropwise into the N_3-PEG_4-COOH solution. The reaction was stirred overnight at 37°C. The solution was dialyzed with a 14 kDa cellulose membrane against NaCl 0.1 M for 1 day and then against Milli-Q water for 2 days. The obtained azidated gelatin ($GELN_3$) was lyophilized and stored at −20°C before use.

4.5 | Azide and α-NeuNAc-(2→3)-β-D-Gal-Functionalized Gelatin ($GELN_3$-3′SialGal)

Gelatin functionalized with both azide and α-NeuNAc-(2→3)-β-D-Gal- was prepared as reported in [64]. Briefly, N_3-PEG_4-COOH (50 mg, 0.17 mmol) was dissolved in PBS 5.5 (3 mL) in a bottom round flask at rt. Then, EDC (66 mg, 0.34 mmol) and NHS (40 mg, 0.34 mmol) were added under gentle stirring. Meanwhile, gelatin type A (250 mg, 0.5 equivalents of lysines with respect to N_3-PEG_4-COOH) was dissolved in PBS 5.5 (10 mL) in a falcon at 37°C. After 30 min, the gelatin solution was added dropwise into the PEG solution. The reaction was stirred overnight at 37°C. The day after, 5.6 g (8.5 mmol, 100 equivalents per lysine residue of gelatin) of α-NeuNAc-(2→3)-β-D-Gal-(1→4)-D-Glc were added to the gelatin solution. After 30 min, $NaBH_3CN$ (293 mg, 4.2 mmol) was added, and the solution was stirred at 37°C overnight. The solution was dialyzed with a 14 kDa cellulose membrane against NaCl 0.1 M for 1 day and then against Milli-Q water for 2 days. The obtained azidated gelatin ($GELN_3$-3'SialGal) was lyophilized and stored at −20°C before use.

4.6 | Biomaterials Characterizations

FTIR. FT-IR analysis was performed using a Nicolet iS20, Thermo Scientific, after freeze drying, 30 scans were acquired for each sample.

NMR.^{1}H NMR analysis was performed using a Varian Mercury 400 M Hz, dissolving the sample in D_2O with 0.05 % (wt.%) TMSP at a concentration of 7 mg/mL.^{13}C NMR analysis was performed using a Varian Mercury 400 M Hz, dissolving the sample in D2O with 0.05 % (wt.%) TMSP at a concentration of 50 mg/mL.

4.7 | Inks Formulation

In this section, the term ink refers to the hydrogel formulation prepared without the incorporation of cells.

$GELN_3$ (26 mg) was dissolved in filtered PBS 7.4 (0.4 mL) at 37°C, 1200 rpm, for 30 min. HAN3 (4 mg) was dissolved in filtered PBS 7.4 (0.5 mL) at 37°C, 1200 rpm, for 2 h and then mixed with the gelatin solution. 4arm-PEG-DBCO (8 mg) dissolved in filtered PBS 7.4 (0.1 mL) was added, and the solution was vortex for 1 min at 1200 rpm until complete gelation occurred. In this way, the ink defined as HA-GEL was obtained.

$GELN_3$-3'SialGal (26 mg) was dissolved in filtered PBS 7.4 (0.4 mL) at 37°C, 1200 rpm, for 30 min. HAN_3 (4 mg) was dissolved in filtered PBS 7.4 (0.5 mL) at 37°C, 1200 rpm, for 2 h and then mixed with the gelatin solution. Then 4arm-PEG-DBCO (8 mg) dissolved in sterile PBS 7.4 (0.1 mL) was added, and the solution was vortex for 1 min at 1200 rpm until complete gelation occurred. In this way, the ink defined as HA-GEL-3'SialGal was obtained.

$GELN_3$ (23 mg) was dissolved in filtered PBS 7.4 (0.2 mL) at 37°C, 1200 rpm, for 30 min. HAN_3 (4 mg) was dissolved in filtered PBS 7.4 (0.5 mL) at 37°C, 1200 rpm, for 2 h. CSN_3 (3 mg) was dissolved in filtered PBS 7.4 (0.2 mL) at 37°C, 1200 rpm for 2 h. The solution

of $GELN_3$ and CSN_3 was added to the HAN_3 solution. Then 4arm-PEG-DBCO (8 mg) dissolved in filtered PBS 7.4 (0.1 mL) was added, and the solution was vortex for 1 min at 1200 rpm until complete gelation occurred. In this way, the ink defined as HA-GEL-CS was obtained.

$GELN_3$-3'SialGal (23 mg) was dissolved in filtered PBS 7.4 (0.2 mL) at 37°C, 1200 rpm, for 30 min. HAN_3 (4 mg) was dissolved in filtered PBS 7.4 (0.5 mL) at 37°C, 1200 rpm, for 2 h. CSN_3 (3 mg) was dissolved in filtered PBS 7.4 (0.2 mL) at 37°C, 1200 rpm for 2 h. The solution of $GELN_3$ and CSN3 was added to the HAN_3 solution. Then 4arm-PEG-DBCO (8 mg) dissolved in sterile PBS 7.4 (0.1 mL) was added, and the solution was vortex for 1 min at 1200 rpm until complete gelation occurred. In this way, the ink defined as HA-GEL-3'SialGal-CS was obtained.

4.8 | 3D Printing

Extrudability and 3D printing accuracy of predicted hydrogel formulations were tested with a BIOX 3D printer (CELLINK). All formulations were printed in a 24-well plate with a pneumatic preheated at 37°C. A 3 mL syringe was equipped with a 22 G conical nozzle (CELLINK). The printing speed was set to 10 mm/s. Pictures of the 3D constructs were taken with a digital camera right after printing. A drop test was performed for each formulation in order to determine the optimal printing pressure (i.e., the pressure at which the ink started to flow constantly throughout the nozzle).

4.9 | Swelling Test

1 mL of hydrogel for each formulation (HA-GEL, HA-GEL-3'SialGal, HA-GEL-CS, HA-GEL-3'SialGal-CS) was formulated into 3 plastic vials (diameter 10 mm), 0.3 mL each, before gelation occur. The hydrogel was then rinsed with 1 mL of PBS at physiological pH (7.4) containing 0.02% w/V NaN_3 as a preservative. The vials were weighed to determine their tare mass and then weighed again with the hydrogel to assess the initial hydrogel amount in each tube. The percentage of absorbed water was calculated experimentally by subtracting the hydrogel mass at a specific time point from the initial hydrogel mass and normalizing by dividing by the initial hydrogel mass [64]:

$$\text{Absorbed water mass (t)} = (\text{hydrogel mass (t)} - \text{initial mass}) / \text{initial mass}$$

Hydrogels were weighed at regular intervals, removing and replacing the volume of PBS. Samples were tested both at physiological pH (7.4) and weakly acidic pH (5.5).

4.10 | SEM

SEM analyses were performed using a ZEISS Gemini 500 SEM, with an acceleration voltage of 3 kV and an In-Lens detector. The hydrogels were frozen at −80°C for 24 h and lyophilized. Samples were placed on a metal support using a carbon disc and subsequently coated with gold using an Edwards Sputter Coater S150B.

4.11 | Cell Culture

Human glioma U87-MG cells were cultured in Dulbecco's modified Eagle's medium supplemented with 10% fetal bovine serum, 100 units/ml penicillin, and 100 mg/ml streptomycin at 37°C under a humidified atmosphere with 5% CO2. Cells were grown to 90% confluence, trypsinized, plated in 75 cm^2 culture dishes at a density of 1×10^6 cells, and incubated at 37°C in a humidified atmosphere containing 5% CO2. The media was changed every two-three days.

A glioma stem cell line was used for the analysis: G166. It was provided by Professor A. Smith of the Wellcome Trust Medical Research Council Stem Cell Institute, University of Cambridge, Cambridge (UK). The cells are cultured under selective conditions that maintain their stem-like properties, using an optimized medium composed of DMEM F-12 (Euroclone S.p.A.) and Neurobasal (Life Technologies Italia, Milan, Italy) 1:1, B-27 Supplement without vitamin A (Life Technologies Italia, Milan, Italy), 2 mM L-glutamine (Euroclone S.p.A., Milan, Italy), 20 ng/mL recombinant human EGF and 10 ng/mL recombinant human bFGF (Milteny Biotec, Bergish Gladbach, Germany), 20 UI/mL penicillin and 20 μg/mL streptomycin (Euroclone S.p.A., Milan, Italy) [5]. The laminin (Merck Life Sciences S.r.l.) coating allows the cells to grow adherent to the support in a monolayer. Cells are cultured at 37°C and 5% CO2 humidified incubator. This cell line has been authenticated using Short Tandem Repeat profiling (Supplementary Table S5).

4.12 | Bioinks Formulation

In this section, the term *bioink* refers to the hydrogel formulation prepared with the incorporation of cells into the previously described inks.

HA-GEL bionik. $GELN_3$ (26 mg) was dissolved in filtered 0.3 mL PBS 7.4 at 37°C and HAN_3 (4 mg) in 0.5 mL PBS 7.4. Solutions were sterilized under UV light for 30 min. 4arm-PEG-DBCO powder (8 mg) was sterilized under UV light for 30 min before dissolution in 0.1 mL sterile PBS 7.4. HA and $GELN_3$ solutions were mixed for bioprinting, adding 2×10^6 U87 or G166 cells suspended in 0.1 mL PBS. Finally, 4arm-PEG-DBCO was added, and the mixtures were loaded in the bioprinter syringe. The bioink was bioprinted after 2 min at 40 kPa with a 22G conical bioprinter nozzle with Cellink INKREDIBLE 3D bioprinter in a 24-well plate and each well was rinsed with 0.7 mL of medium.

HA-GEL-3'SialGal bioink. $GELN_3$-3'SialGal (26 mg) was dissolved in filtered 0.3 mL PBS 7.4 at 37°C and HAN_3 (4 mg) in 0.5 mL PBS 7.4. Solutions were sterilized under UV light for 30 min. 4arm-PEG-DBCO powder (8 mg) was sterilized under UV light for 30 min before dissolution in 0.1 mL sterile PBS 7.4. HA and $GELN_3$-3'SialGal solutions were mixed for bioprinting, adding 2×10^6 U87 or G166 cells suspended in 0.1 mL PBS. Finally, 4arm-PEG-DBCO was added, and the mixtures were loaded in

the bioprinter syringe. The bioink was bioprinted after 2 min at 40 kPa with a 22G conical bioprinter nozzle with Cellink INKREDIBLE 3D bioprinter in a 24-well plate and each well was rinsed with 0.7 mL of medium.

HA-GEL-CS bionik. $GELN_3$ (23 mg) was dissolved in filtered 0.2 mL PBS 7.4 at 37°C, HAN_3 (4 mg) in 0.5 mL PBS 7.4, and CSN_3 (3 mg) in 0.2 mL PBS 7.4. Solutions were sterilized under UV light for 30 min. 4arm-PEG-DBCO powder (8 mg) was sterilized under UV light for 30 min before dissolution in 0.1 mL sterile PBS 7.4. HA, $GELN_3$, and CSN_3 solutions were mixed for bioprinting, adding 2×10^6 U87 or G166 cells suspended in 0.1 mL PBS. Finally, 4arm-PEG-DBCO was added, and the mixtures were loaded in the bioprinter syringe. The bioink was bioprinted after 2 min at 40 kPa with a 22G conical bioprinter nozzle with Cellink INKREDIBLE 3D bioprinter in a 24-well plate and each well was rinsed with 0.7 mL of medium.

HA-GEL-3'SialGal-CS bionik. $GELN_3$-3'SialGal (23 mg) was dissolved in filtered 0.2 mL PBS 7.4 at 37°C, HAN_3 (4 mg) in 0.5 mL PBS 7.4, and CSN_3 (3 mg) in 0.2 mL PBS 7.4. Solutions were sterilized under UV light for 30 min. 4arm-PEG-DBCO powder (8 mg) was sterilized under UV light for 30 min before dissolution in 0.1 mL sterile PBS 7.4. HA, $GELN_3$-3'SialGal, and CSN_3 solutions were mixed for bioprinting, adding 2×10^6 U87 or G166 cells suspended in 0.1 mL PBS. Finally, 4arm-PEG-DBCO was added, and the mixtures were loaded in the bioprinter syringe. The bioink was bioprinted after 2 min at 40 kPa with a 22G conical bioprinter nozzle with Cellink INKREDIBLE 3D bioprinter in a 24-well plate and each well was rinsed with 0.7 mL of medium.

4.13 | LIVE/DEAD and Alamar Blue Assay

The viability of 3D cell-laden hydrogels was investigated with a live/dead Cell viability Assay kit. U87 were bioprinted inside the hydrogels in a 24-well plate. At 14 days, U87 were stained with green-fluorescent calcein-AM to indicate intracellular esterase activity for 1 h (37°C, 5% CO2). Fluorescence images were collected with CellObserved Microscopy.

The viability of 3D cell-laden hydrogels was also investigated with the Alamar Blue assay (Invitrogen). U87 cell-laden hydrogels were bioprinted on a 24-well plate. On 1, 3, 7, and 14 days, samples were incubated with 10% Alamar Blue reagent in medium. After 2 h, 0,1 mL condition medium was collected, and the absorbance was measured at 570 and 600 nm wavelengths. Percentage viability was finally calculated using Equation:

$$Red_{AlamarB}\% = \frac{(O_2 \times A_1) - (O_1 \times A_2)}{(R_1 \times N_2) - (R_2 \times N_1)} \times 100$$

Eq. Formula for cell viability, where O1 and O2 are the molar extinction coefficients of oxidized Alamar Blue reagent at 570 (80586) and 600 nm (117216) respectively, A570 and A600 are absorbances of test wells at 570 and 600 nm respectively, R1 and R2 are the molar extinction coefficients of reduced Alamar Blue reagent at 570 (155677) and 600 nm (14652) and N1 and N2 are absorbances of negative control wells (media plus Alamar Blue without cells) at 570 and 600 nm respectively [65].

4.14 | Drug Testing

After 7 days of culture, G166 cells embedded in the four 3D bioprinted formulations (HA-GEL, HA-GEL-3'SialGal, HA-GEL-CS, HA-GEL-3'SialGal-CS) were treated for 3 days. For each formulation, treatments consisted of: (i) 200 μM temozolomide (TMZ); (ii) 25 μM MV1035; (iii) a combination of 200 μM TMZ and 25 μM MV1035; or (iv) 90 mM DMSO (vehicle control). Post-treatment, samples were fixed in 4% PFA for 1 h, stained with pink alcohol for tracking, and embedded in paraffin blocks for histological analysis.

4.15 | Computational Analysis of Glycosignature-Associated Genes

A curated panel of glycosignature- and GBM-associated genes was analysed using publicly available transcriptomic and clinical datasets from TCGA/PanCancerAtlas and CPTAC, according to dataset availability. The gene panel includes markers related to hyaluronic acid metabolism, chondroitin sulfate synthesis and remodeling, sialylation pathways, ECM organization, glioma stemness, proliferation, hypoxia, invasion, and therapy resistance.

Gene expression distributions were visualized for available genes in each dataset. Survival associations were explored using Cox proportional hazards models implemented in R. The available multivariate models included age and gender as clinical covariates. Complete gene lists, expression plot indices, and exported statistical outputs are provided in the Supporting Information.

4.16 | Multiplex Immunofluorescence

4 μM sections of a paraffin-embedded sample were analyzed. Multiplex staining was carried out according to the MILAN protocol [66], as previously reported [67]. The method consists of repeated cycles of indirect immunofluorescent staining using unconjugated primary antibodies and fluorophore-conjugated secondary antibodies (Table S3), followed by image acquisition and antibody stripping with a detergent and reducing agent. Slides were counterstained with DAPI for nuclear visualization and incubated with secondary antibodies conjugated to three fluorophores, Alexa Fluor 488, Cy3, and Alexa Fluor 647, to detect all target antigens.

Image acquisition and processing were performed using the THUNDER Imager Tissue microscope and LAS X software (Leica Microsystems, Wetzlar, Germany). The full tissue was initially scanned with the HC PL APO 10×/0.45 DRY objective to obtain an overview image. This overview was subsequently used to identify individual cores, enabling sequential high-resolution imaging of selected cores with the HC PL APO 20×/0.80 DRY objective.

Spatial proteomics images were analyzed using the HALO platform (Indica Labs, version 3.6.4134.137). Multiplex fluorescence analysis was performed with the Highplex FL module (Indica Labs), allowing the simultaneous quantification of markers. Marker-specific intensity thresholds were defined to classify cells as either positive or negative for each marker.

Statistical analyses and graphical representations were performed using Python software (version 3.14). Fluorescence intensity data were normalized and compared across treatment conditions and ECM compositions. Differential marker expression was assessed by calculating median differences and double-delta variations relative to the HA-GEL reference condition. Statistical significance was expressed as −log10(p) values, with significance thresholds defined as $p < 0.05$, $p < 0.01$, and $p < 0.001$.

Bubble plots and bar plots were generated to visualize marker expression profiles across experimental conditions, including DMSO, TMZ, MV1035, and TMZ-MV1035 treatments. Z-score normalization was additionally applied for phenotype-oriented analyses, allowing the identification of relative increases or decreases in proliferation and stemness/resistance-associated markers among the different matrices and treatment groups.

4.17 | X-ray Nano-Holotomography (XNH-CT)

X-ray nano-holotomography (XNH-CT) measurements were carried out at the Nano-imaging beamline ID16A of the European Synchrotron Radiation Facility (ESRF, Grenoble, France). This beamline is designed for nanometric spatial resolution 3D holographic (and thus quantitative) 3D x-ray imaging. The beamline is 185m long, and, via a pair of multilayer-coated Kirkpatrick-Baez mirrors [68], provides nano-focused (spot size ∼25 × 30 nm^2) monochromatic beams at either ∼17 or ∼33 keV, with flux in the order of 10^{14} photons/s unfiltered, 10^{11} photons/s after filtering. In addition to standard sample fixation, cryogenic sample preservation is also available. The beam has a cone geometry, and the XNH-CT setup consists of a vacuum chamber within which a high-precision translation and rotation sample stage is installed for alignment and tomographic acquisitions. For XNH-CT, the sample is positioned at usually 4 sample-to-detector (defocusing) distances (calculated depending on the needed pixel size) and, at each of them, a set of projection images is collected over 180 degrees in either 'step-by-step' or 'continuous' modes. Radiographs are recorded by an indirect-conversion Andor Balor camera. The details of this setup are well-described in [63].

In this study, data were acquired in vacuum with 33.3 keV x-rays (electron ring current of 200 mA) in 'step-by-step' mode to guarantee best quality images. This allows using a randomized sample displacement between projections, enabling suppression of artefacts due to structured inhomogeneities within the x-ray beam. All samples were examined by acquiring first a low-resolution, single-distance overview CT scan with a voxel size of 180^3 nm^3 that was used to locate the regions of interest to be imaged by XNH-CT with a voxel size of 100^3 or 50^3 nm^3. XNH-CT dataset consists of 2000 projections, each acquired with an exposure time of 200 ms. These high spatial resolutions were used to characterize the ECM in both distal and core regions by targeting areas in which the density of ECM is indicative of both composition and organization of the matrix and the interface with cell aggregates. At this resolution, information on the interaction between cells and neoproduced ECM and ECM mimics (100 nm – 1 μM) can be accessed. The scope is to study ECM and cell organization in response to the drug treatments. Samples used for these measurements were stained with pink alcohol and embedded in paraffin. Rods were punched out with a biopsy punch of 750 μM in diameter and then glued on metal pins and holders to be mounted on the sample stage.

XNH-CT data were processed using the workflow implemented at ID16a, which brings raw projections from 4 different CT sets to one 3D phase-contrast volume. Radiographs are normalized with respect to the incoming x-ray beam, and then the different sample-to-detector-distance datasets acquired in cone-beam geometry are brought to the same image magnification and aligned. The reconstruction pipeline consists of phase retrieval and tomographic reconstruction, utilizing ESRF-developed software implemented in both Octave and Python environments. Overview CT data were reconstructed after application of the single-distance Paganin's phase-retrieval algorithm (Paganin-length parameter: 100) [69]. The multi-distance acquisition enables accurate phase retrieval by using an adapted contrast transfer function to recover initial phase maps of the object [70] that are then refined through an iterative non-linear conjugate gradient optimization process, typically converging after ten iterations [71].

Tomographic reconstruction of the retrieved phase maps is performed using Nabu, an open-source Python-based framework developed at the ESRF (https://gitlab.esrf.fr/tomotools/nabu). Nabu supports both filtered back-projection (FBP) and iterative reconstruction techniques, alongside advanced post-processing tools such as ring artifact correction based on the combined wavelet–Fourier method introduced by [72]. In this study, all reconstructions used the FBP algorithm for consistency across datasets. GPU acceleration was employed to efficiently handle the large-scale datasets typical of nano-holotomography. The reconstructed volumes were automatically converted into the standardized NeXus (NX) file format to support reproducibility, long-term data preservation, and seamless integration with downstream analysis workflows.

To further enhance image quality, post-processing was applied to reduce noise, which is commonly present in phase-contrast reconstructions. A bilateral filter was used to denoise the images while preserving edges and fine structural details. Unlike conventional linear filters, the bilateral filter considers both spatial proximity and intensity similarity, enabling effective noise suppression without blurring critical features [73]. We implemented this filtering step using the cv2.bilateralFilter function from the OpenCV Python package, carefully selecting the parameters to balance noise reduction and edge preservation (e.g., d = 8, sigmaColor = 75, sigmaSpace = 75). This step significantly improved the interpretability of soft tissue boundaries and microstructural features in the samples, thereby ensuring the reliability of subsequent quantitative analyses. All parameters used in the different steps of the data processing pipeline are stored as 'Scientific Metadata' in the LMU SciCat catalogue. These metadata parameters can be accessed upon request to the LMU authors, ensuring transparency and reproducibility of the workflow [74].

To quantify the grayscale intensity (Figure 5C,D) as a proxy for matrix density surrounding the cell clusters, a custom interactive image analysis script was developed in Python. For each sample volume, three distinct tomographic slices were selected. Within each slice, three cell clusters were identified, and an interactive

region of interest (ROI) was defined around each cluster using a circular mask with a fixed radius of 20 pixels (corresponding to a diameter of 4 μM) to analyze the immediate pericellular matrix deposition.

The software calculated the mean pixel intensity within each individual circular ROI directly from the raw image data to avoid interpolation of artifacts. A total of 9 ROIs per sample (3 slices x 3 clusters) were analyzed. The intensity values were then averaged for each sample, and the results were expressed as mean ± standard deviation.

The structural dimension of the cell clusters (Figure 5E) was quantified using ImageJ software. Spatial calibration was performed according to the image metadata (10 pixel/μM). The diameter of the cell clusters was manually measured across three representative slices per sample, selecting three distinct clusters per slice. The dimensional data were compiled to compute the final mean and standard deviation for each experimental group.

4.18 | Statistical Analysis

Data were always presented as mean ± standard deviation, unless otherwise specified. Values were averaged from at least three repeated measurements ($n = 3$). To determine statistical difference between two groups or more groups was done with one-way ANOVA using Tukey's multiple-comparison test. Statistical significance of the data was calculated at 95% ($p < 0.05$) confidence intervals. Non-significant (ns), $p > 0.05$, * $p \leq 0.05$, ** $p \leq 0.01$, *** $p \leq 0.001$, **** $p \leq 0.0001$.

Acknowledgements

The research leading to these results has received funding from AIRC under MFAG 2025 - ID. 31886 project P.I. Ramazzotti Daniele and the European Union—NextGenerationEU through the Italian Ministry of University and Research under PNRR—M4C2-I1.3 Project PE00000019 "HEAL ITALIA" to Alberto Bravin and Sobhan Sheikhi—CUP H43C22000830006. This work was funded by the National Plan for NRRP Complementary Investments (PNC, established with the decree-law 6 May 2021, n. 59, converted by law n. 101 of 2021) in the call for the funding of research initiatives for technologies and innovative trajectories in the health and care sectors (Directorial Decree n. 931 of 06-06-2022)—project n. PNC0000003 – AdvaNced Technologies for Human-centrEd Medicine (project acronym: ANTHEM). CUP BICOCCA B53C22006670001; CIG: BC3A616A21. This work reflects only the authors' views and opinions; neither the Ministry for University and Research nor the European Commission can be considered responsible for them. Financial support from: Ministero della Salute, RF-2021-12371959 Tackling immunomodulatory properties of stromal cells to improve therapeutic strategies in lung cancer. MUR PRIN 2022, 2022MY7AZT Dynamic multifunctional hydrogels for glioblastoma therapy (DINGO). This publication was also written in the context of the work of the consortium DAPHNE4NFDI in association with the German National Research Data Infrastructure (NFDI) e.V. NFDI is financed by the Federal Republic of Germany and the 16 federal states, and the consortium is funded by the Deutsche Forschungsgemeinschaft (DFG, German Research Foundation)—project number 460248799. Paola Coan and Hafiz Fahad would like to thank the funding and support. Furthermore, thanks go to all institutions and actors who are committed to the association and its goals. This work was funded by Fondazione Cariplo 2024-NAZ-0094 CUP BICOCCA H45E24000440007. We acknowledge the European Synchrotron Radiation Facility (ESRF) for provision of synchrotron radiation facilities under proposal ID LS3379 and LS3548 and on beamline ID16a.

Open access publishing facilitated by Universita degli Studi di Milano-Bicocca, as part of the Wiley - CRUI-CARE agreement.

Conflicts of Interest

The authors declare no conflicts of interest.

Data Availability Statement

The data that support the findings of this study are openly available in Zenodo at [10.5281/zenodo.20426371]. The Synchrotron experimental data supporting the findings of this study have been deposited in the European Synchrotron Radiation Facility (ESRF) data repository. International Generic Sample Numbers (IGSNs): HA-GEL_DMSO-Rep1: https://doi.org/10.60578/gcb0-tyed, HA-GEL_DMSO-Rep2: https://doi.org/10.60578/e53r-je89, HA-GEL_DMSO-Rep3: https://doi.org/10.60578/wv93-ktax, HA-GEL_3'SialGal-CS_DMSO-Rep1: https://doi.org/10.60578/bsre-mfzb, HA-GEL_3'SialGal-CS_DMSO-Rep2: https://doi.org/10.60578/g843-kpvf, HA-GEL_3'SialGal-CS_DMSO-Rep3: https://doi.org/10.60578/kp5x-yeqr, HA-GEL_TMZ-Rep1: https://doi.org/10.60578/dgav-wawv, HA-GEL_TMZ-Rep2: https://doi.org/10.60578/h4up-7kjz, HA-GEL_TMZ-Rep3: https://doi.org/10.60578/n3uz-9afr, HA-GEL_3'SialGal-CS_TMZ-Rep1: https://doi.org/10.60578/31px-9jhy, HA-GEL_3'SialGal-CS_TMZ-Rep2: https://doi.org/10.60578/6gx3-ufxv, HA-GEL_3'SialGal-CS_TMZ-Rep3: https://doi.org/10.60578/374p-c03x, HA-GEL_MV1035-Rep1: https://doi.org/10.60578/7j2e-mpzy, HA-GEL_MV1035-Rep2: https://doi.org/10.60578/a60r-va5w, HA-GEL_MV1035-Rep3: https://doi.org/10.60578/pbnk-n8jh, HA-GEL_3'SialGal-CS_MV1035-Rep1: https://doi.org/10.60578/bmwn-d6nv, HA-GEL_3'SialGal-CS_MV1035-Rep2: https://doi.org/10.60578/dr19-8k0h, HA-GEL_3'SialGal-CS_MV1035-Rep3: https://doi.org/10.60578/7my7-ddjn, HA-GEL_TMZ_M1035-Rep1: https://doi.org/10.60578/b0d3-7j3d, HA-GEL_TMZ_M1035-Rep2: https://doi.org/10.60578/4cqn-phsz, HA-GEL_TMZ_M1035-Rep3: https://doi.org/10.60578/cahg-4n5x, HA-GEL_3'SialGal-CS_TMZ_MV1035-Rep1: https://doi.org/10.60578/w32f-tnt7, HA-GEL_3'SialGal-CS_TMZ_MV1035-Rep2: https://doi.org/10.60578/0jf7-3tu6, HA-GEL_3'SialGal-CS_TMZ_MV1035-Rep3: https://doi.org/10.60578/jquf-yh0n.

References

1. J. L. Shah, G. H. Li, and S. G. Soltys, "Glioblastoma Multiforme," *CyberKnife Stereotactic Radiosurgery: Brain* 1 (2024): 85–98, https://doi.org/10.22290/jbnc.v24i1.1481.

2. M. E. Davis, "Glioblastoma: Overview Of Disease And Treatment," *Clinical Journal of Oncology Nursing* 20, no. 5 (2016): S2–S8, https://doi.org/10.1188/16.CJON.S1.2-8.

3. S. Singh, D. Dey, D. Barik, et al., "Glioblastoma At The Crossroads: Current Understanding And Future Therapeutic Horizons," *Signal Transduction and Targeted Therapy* 10, no. 1 (2025): 213, https://doi.org/10.1038/s41392-025-02299-4.

4. V. Zoi, V. Galani, C. Sioka, G. A. Alexiou, and A. P. Kyritsis, "Immunotherapy for Glioblastoma: A Focus on PD-1/PD-L1 Inhibitors," *Cancers* 17, no. 23 (2025): 3777, https://doi.org/10.3390/CANCERS17233777.

5. R. Stupp, W. P. Mason, M. J. van den Bent, et al., "Radiotherapy plus Concomitant and Adjuvant Temozolomide for Glioblastoma," *New England Journal of Medicine* 352, no. 10 (2005): 987–996, https://doi.org/10.1056/NEJMOA043330;PAGE:STRING:ARTICLE/CHAPTER.

6. F. Loebel, C. V. Sánchez, L. B. Alvarez, et al., "Profiles Of Survival Prediction In Glioblastoma," *Brain and Spine* 5 (2025): 104324, https://doi.org/10.1016/J.BAS.2025.104324.

7. H. Piyadasa, B. Oberlton, M. Ribi, et al., "Multi-Omic Landscape Of Human Gliomas From Diagnosis To Treatment And Recurrence," *Cancer Cell* 0, no. 0 (2025): 1–17, https://doi.org/10.1016/J.CCELL.2025.11.006.

8. T. Zhao, H. Ge, C. Lin, X. Wu, and J. Chen, "Glycosylation Gene Signatures As Prognostic Biomarkers In Glioblastoma," *Annals of Clinical and Translational Neurology* 12, no. 7 (2025): 1378–1394, https://doi.org/10.1002/ACN3.70068;JOURNAL:JOURNAL:23289503;WGROUP:STRING:PUBLICATION.

9. W.-C. Liao, C.-K. Liao, T.-J. Tseng, et al., "Chondroitin Sulfate Synthase 1 Enhances Proliferation Of Glioblastoma By Modulating PDGFRA Stability," *Oncogenesis* 9, no. 2 (2020): 9, https://doi.org/10.1038/s41389-020-0197-0.

10. U. Kuliesiute, K. Joseph, J. Straehle, et al., "Sialic Acid Metabolism Orchestrates Transcellular Connectivity And Signaling In Glioblastoma," *Neuro-Oncology* 25, no. 11 (2023): 1963–1975, https://doi.org/10.1093/NEUONC/NOAD101.

11. P. Schmassmann, J. Roux, A. Buck, et al., "Targeting The Siglec–Sialic Acid Axis Promotes Antitumor Immune Responses In Preclinical Models Of Glioblastoma," *Science Translational Medicine* 15, no. 705 (2023): adf5302, https://doi.org/10.1126/SCITRANSLMED.ADF5302/ASSET/9B1A405E-B11C-4648-B50A-8EE820C22AB4/ASSETS/IMAGES/LARGE/SCITRANSLMED.ADF5302-F7.JPG.

12. M. Mellai, C. Casalone, C. Corona, et al., "Chondroitin Sulphate Proteoglycans in the Tumour Microenvironment," *Advances in Experimental Medicine and Biology* 1272 (2020): 73–92, https://doi.org/10.1007/978-3-030-48457-6_5.

13. M. Piazzoni, I. Borghi, F. Cadamuro, et al., "Endothelial Cells Angiogenesis in Sulfated Glycosaminoglycan (GAG) Hydrogels Enhanced by Bioactive Glass-Released Ions," *Advanced Functional Materials* 36, no. 30 (2025): 19933, https://doi.org/10.1002/ADFM.202519933;ISSUE:ISSUE:DOI.

14. Y. Mei, X. Wang, J. Zhang, et al., "Siglec-9 Acts As An Immune-Checkpoint Molecule On Macrophages In Glioblastoma, Restricting T-Cell Priming And Immunotherapy Response," *Nature Cancer* 4, no. 9 (2023): 1273–1291, https://doi.org/10.1038/s43018-023-00598-9.

15. R. Wieboldt, M. Sandholzer, E. Carlini, et al., "Engagement Of Sialylated Glycans With Siglec Receptors On Suppressive Myeloid Cells Inhibits Anticancer Immunity Via CCL2," *Cellular & Molecular Immunology* 21, no. 5 (2024): 495–509, https://doi.org/10.1038/s41423-024-01142-0.

16. N. R. Mantuano and H. Läubli, "Sialic Acid And Siglec Receptors In Tumor Immunity And Immunotherapy," *Seminars in Immunology* 74–75 (2024): 101893, https://doi.org/10.1016/J.SMIM.2024.101893.

17. B. W. S. Phon, M. N. A. Kamarudin, S. Bhuvanendran, and A. K. Radhakrishnan, "Transitioning Pre-Clinical Glioblastoma Models To Clinical Settings With Biomarkers Identified In 3D Cell-Based Models: A Systematic Scoping Review," *Biomedicine & Pharmacotherapy* 145 (2022): 112396, https://doi.org/10.1016/J.BIOPHA.2021.112396.

18. P. Sharma, A. Aaroe, J. Liang, and V. K. Puduvalli, "Tumor Microenvironment In Glioblastoma: Current And Emerging Concepts," *Neuro-Oncology Advances* 5, no. 1 (2023): vdad009, https://doi.org/10.1093/NOAJNL/VDAD009.

19. C. Tondepu and L. Karumbaiah, "Glycomaterials to Investigate the Functional Role of Aberrant Glycosylation in Glioblastoma," *Advanced Healthcare Materials* 11, no. 4 (2021): 2101956, https://doi.org/10.1002/ADHM.202101956.

20. S. Han, S. Kim, Z. Chen, et al., "3D Bioprinted Vascularized Tumour for Drug Testing," *International Journal of Molecular Sciences* 21, no. 8 (2020): 2993, https://doi.org/10.3390/IJMS21082993.

21. L. Orcheston-Findlay, S. Bax, R. Utama, M. Engel, D. Govender, and G. O'neill, "Advanced Spheroid, Tumouroid and 3D Bioprinted In-Vitro Models of Adult and Paediatric Glioblastoma," *International Journal of Molecular Sciences* 22, no. 6 (2021): 2962, https://doi.org/10.3390/IJMS22062962.

22. C. Parra-Cantu, W. Li, A. Quiñones-Hinojosa, and Y. S. Zhang, "3D Bioprinting Of Glioblastoma Models," *Journal of 3D Printing in Medicine* 4, no. 2 (2020): 113–125, https://doi.org/10.2217/3DP-2019-0027.

23. S. Bom, R. Ribeiro, H. M. Ribeiro, C. Santos, and J. Marto, "On The Progress Of Hydrogel-Based 3D Printing: Correlating Rheological Properties With Printing Behaviour," *International Journal of Pharmaceutics* 615 (2022): 121506, https://doi.org/10.1016/J.IJPHARM.2022.121506.

24. S. M. Hull, L. G. Brunel, and S. C. Heilshorn, "3D Bioprinting of Cell-Laden Hydrogels for Improved Biological Functionality," *Advanced Materials* 34, no. 2 (2022): 2103691, https://doi.org/10.1002/ADMA.202103691;PAGE:STRING:ARTICLE/CHAPTER.

25. F. Cadamuro, M. Piazzoni, E. Gamba, et al., "Artificial Intelligence Tool For Prediction Of ECM Mimics Hydrogel Formulations Via Click Chemistry," *Biomaterials Advances* 175 (2025): 214323, https://doi.org/10.1016/J.BIOADV.2025.214323.

26. M. S. A. Mier, E. Türker, J. Faber, et al., "3D In Vitro Glioma-Neuron-Astrocyte Biomimetic Composites Recapitulate Key Molecular Mechanisms Linked to Glioblastoma Multiforme Pathophysiology," *Advanced Functional Materials* 35, no. 22 (2025): 2419211, https://doi.org/10.1002/ADFM.202419211.

27. L. J. Smith, A. Skirzynska, A. A. Chin, et al., "Engineered In Vitro Tumor Model Recapitulates Molecular Signatures of Invasion in Glioblastoma," *ACS Materials Au* 3, no. 5 (2023): 514–527, https://doi.org/10.1021/ACSMATERIALSAU.3C00029/ASSET/IMAGES/LARGE/MG3C00029_0005.JPEG.

28. C. Tondepu and L. Karumbaiah, "Glycomaterials to Investigate the Functional Role of Aberrant Glycosylation in Glioblastoma," *Advanced Healthcare Materials* 11, no. 4 (2022): 2101956, https://doi.org/10.1002/ADHM.202101956;WEBSITE:WEBSITE:ADVANCED;ISSUE:ISSUE:DOI.

29. H. A. Cuello, G. M. Ferreira, C. A. Gulino, A. G. Toledo, V. I. Segatori, and M. R. Gabri, "Terminally Sialylated And Fucosylated Complex N-Glycans Are Involved In The Malignant Behavior Of High-Grade Glioma," *Oncotarget* 11, no. 52 (2020): 4822–4835, https://doi.org/10.18632/ONCOTARGET.27850.

30. Y.-C. Lin, Y.-H. Chu, W.-C. Liao, et al., "CHST11-Modified Chondroitin 4-Sulfate As A Potential Therapeutic Target For Glioblastoma," *American Journal of Cancer Research* 13, no. 7 (2023): 2998.

31. W. Zheng, H. Zhang, Y. Huo, et al., "The Role Of ST3GAL4 in Glioma Malignancy, Macrophage Infiltration, And Prognostic Outcomes," *Heliyon* 10, no. 9 (2024): 29829, https://doi.org/10.1016/J.HELIYON.2024.E29829.

32. F. Cadamuro, F. Nicotra, and L. Russo, "3D Printed Tissue Models: From Hydrogels To Biomedical Applications," *Journal of Controlled Release* 354 (2023): 726–745, https://doi.org/10.1016/J.JCONREL.2023.01.048.

33. L. Nie, Y. Sun, O. V. Okoro, Y. Deng, G. Jiang, and A. Shavandi, "Click Chemistry For 3D Bioprinting," *Materials Horizons* 10, no. 8 (2023): 2727–2763, https://doi.org/10.1039/D3MH00516J.

34. Y. Huang, P. B. Jayathilaka, M. S. Islam, et al., "Structural Aspects Controlling The Mechanical And Biological Properties Of Tough, Double Network Hydrogels," *Acta Biomaterialia* 138 (2022): 301–312, https://doi.org/10.1016/J.ACTBIO.2021.10.044.

35. M. S. A. Mier, E. Türker, J. Faber, et al., "3D In Vitro Glioma-Neuron-Astrocyte Biomimetic Composites Recapitulate Key Molecular Mechanisms Linked to Glioblastoma Multiforme Pathophysiology," *Advanced Functional Materials* 35 (2025): 2419211, https://doi.org/10.1002/ADFM.202419211;CSUBTYPE:STRING:AHEAD.

36. L. Karumbaiah, S. F. Enam, A. C. Brown, et al., "Chondroitin Sulfate Glycosaminoglycan Hydrogels Create Endogenous Niches for Neural Stem Cells," *Bioconjugate Chemistry* 26, no. 12 (2015): 2336–2349, https://doi.org/10.1021/ACS.BIOCONJCHEM.5B00397/ASSET/IMAGES/BC-2015-00397M_M001.GIF.

37. Y. T. Tung, Y. C. Chen, K. Derr, K. Wilson, M. J. Song, and M. Ferrer, "A 3D Bioprinted Human Neurovascular Unit Model of Glioblastoma Tumor Growth," *Advanced Healthcare Materials* 13, no. 15 (2024): 2302831, https://doi.org/10.1002/ADHM.202302831;WGROUP:STRING:PUBLICATION.

38. F. Bojin, A. Robu, M. I. Bejenariu, et al., "3D Bioprinting Of Model Tissues That Mimic The Tumor Microenvironment," *Micromachines* 12, no. 5 (2021): 535, https://doi.org/10.3390/MI12050535/S1.

39. Y. Liu, S. Wang, D. Sun, et al., "Development of a Biomimetic Chondroitin Sulfate-modified Hydrogel to Enhance the Metastasis of Tumor Cells," *Scientific Reports* 6, no. 1 (2016): 24761, https://doi.org/10.1038/srep29858.

40. A. Y. Tsidulko, G. M. Kazanskaya, A. M. Volkov, et al., "Chondroitin Sulfate Content And Decorin Expression In Glioblastoma Are Associated With Proliferative Activity Of Glioma Cells And Disease Prognosis," *Cell and Tissue Research* 379, no. 1 (2020): 147–155, https://doi.org/10.1007/S00441-019-03127-2/TABLES/3.

41. M. T. Logun, N. S. Bisel, E. A. Tanasse, et al., "Glioma Cell Invasion Is Significantly Enhanced In Composite Hydrogel Matrices Composed Of Chondroitin 4- And 4,6-Sulfated Glycosaminoglycans4,6-Sulfated Glycosaminoglycans," *Journal of Materials Chemistry B* 4, no. 36 (2016): 6052–6064, https://doi.org/10.1039/C6TB01083K.

42. I. F. Habeeb, T. E. Alao, D. Delgado, and A. Buffone, "When A Negative (Charge) Is Not A Positive: Sialylation And Its Role In Cancer Mechanics And Progression," *Frontiers in Oncology* 14 (2024): 1487306, https://doi.org/10.3389/FONC.2024.1487306/XML/NLM.

43. F. Barbugian, F. Cadamuro, F. Nicotra, C. Riccardi, and L. Russo, "Plasma-Treated Collagen Functionalized With Chondroitin Sulfate as Bioactive and Nanostructured Extracellular Matrix Mimics," *Nanomedicine* 19, no. 9 (2024): 799–810, https://doi.org/10.2217/NNM-2023-0310.

44. A. Malacrida, A. Di Domizio, A. Bentivegna, et al., "MV1035 Overcomes Temozolomide Resistance in Patient-Derived Glioblastoma Stem Cell Lines," *Biology* 11, no. 1 (2022): 70, https://doi.org/10.3390/BIOLOGY11010070/S1.

45. S. Ajarrag and Y. St-Pierre, "Galectins in Glioma: Current Roles in Cancer Progression and Future Directions for Improving Treatment," *Cancers* 13, no. 21 (2021): 5533, https://doi.org/10.3390/CANCERS13215533.

46. G. C. Machado and V. P. Ferrer, "MUC1 And MUC4 Expression Are Inversely Correlated And Trigger Immunological Response And Transport Pathways In Adult-Type Diffuse Gliomas," *Computers in Biology and Medicine* 187 (2025): 109730, https://doi.org/10.1016/J.COMPBIOMED.2025.109730.

47. A. Fidoamore, L. Cristiano, A. Antonosante, et al., "Glioblastoma Stem Cells Microenvironment: The Paracrine Roles of the Niche in Drug and Radioresistance," *Stem Cells International* 2016, no. 1 (2016): 6809105, https://doi.org/10.1155/2016/6809105.

48. E. Codrici, A. M. Enciu, I. D. Popescu, S. Mihai, and C. Tanase, "Glioma Stem Cells and Their Microenvironments: Providers of Challenging Therapeutic Targets," *Stem Cells International* 2016, no. 1 (2016): 5728438, https://doi.org/10.1155/2016/5728438.

49. C. Guetta-Terrier, D. Karambizi, B. Akosman, et al., "CHI3L1 Is a Modulator of Glioma Stem Cell States and a Therapeutic Target in Glioblastoma," *Cancer Research* 83, no. 12 (2023): 1984–1999, https://doi.org/10.1158/0008-5472.CAN-21-3629/726038/AM/CHI3L1-IS-A-MODULATOR-OF-GLIOMA-STEM-CELL-STATES.

50. H. Nada, L. Zhang, B. Kaur, and M. T. Gabr, "CHI3L1-Targeted Small Molecules As Glioblastoma Therapies: Virtual Screening-Based Discovery, Biophysical Validation, Pharmacokinetic Profiling, And Evaluation In Glioblastoma Spheroids," *European Journal of Medicinal Chemistry* 297 (2025): 117960, https://doi.org/10.1016/j.ejmech.2025.117960.

51. Y. K. Chong, E. Sandanaraj, L. W. H. Koh, et al., "ST3GAL1-Associated Transcriptomic Program in Glioblastoma Tumor Growth, Invasion, and Prognosis," *JNCI: Journal of the National Cancer Institute* 326, no. 2 (2016): djv326, https://doi.org/10.1093/jnci/djv326.

52. T. Fukumori, H. Kanayama, and A. Raz, "The Role Of Galectin-3 In Cancer Drug Resistance," *Drug Resistance Updates : Reviews And Commentaries In Antimicrobial And Anticancer Chemotherapy* 10, no. 3 (2007): 101, https://doi.org/10.1016/j.drup.2007.04.001.

53. A. Hara, M. Niwa, T. Kanayama, et al., "Galectin-3: A Potential Prognostic And Diagnostic Marker For Heart Disease And Detection Of Early Stage Pathology," *Biomolecules* 10 (2020): 1277.

54. W. Li, C. Wu, Y. Yao, et al., "MUC4 Modulates Human Glioblastoma Cell Proliferation And Invasion By Upregulating EGFR Expression," *Neuroscience Letters* 566 (2014): 82–87, https://doi.org/10.1016/J.NEULET.2014.02.033.

55. G. C. Machado and V. P. Ferrer, "MUC1 And MUC4 Expression Are Inversely Correlated And Trigger Immunological Response And Transport Pathways In Adult-Type Diffuse Gliomas," *Computers in Biology and Medicine* 187, no. 3 (2025): 109730, https://doi.org/10.1016/j.compbiomed.2025.109730.

56. I. Radziejewska, "Galectin-3 and Epithelial MUC1 Mucin—Interactions Supporting Cancer Development," *Cancers* 15, no. 10 (2023): 2680, https://doi.org/10.3390/cancers15102680.

57. C. Guetta-Terrier, D. Karambizi, B. Akosman, et al., "CHI3L1 Is a Modulator of Glioma Stem Cell States and a Therapeutic Target in Glioblastoma," *Cancer Research* 83, no. 12 (2023): 1984–1999, https://doi.org/10.1158/0008-5472.CAN-21-3629.

58. G. A. Videla-Richardson, O. Morris-Hanon, N. I. Torres, et al., "Galectins as Emerging Glyco-Checkpoints and Therapeutic Targets in Glioblastoma," *International Journal of Molecular Sciences* 23, no. 1 (2021): 316, https://doi.org/10.3390/IJMS23010316.

59. P. Wang, B. Liao, S. Gong, et al., "Temozolomide Promotes Glioblastoma Stemness Expression Through Senescence-Associated Reprogramming Via HIF1α/HIF2α Regulation," *Cell Death & Disease* 16, no. 1 (2025): 317, https://doi.org/10.1038/s41419-025-07617-w.

60. S. Dalfino, E. Olaret, M. Piazzoni, et al., "Polycaprolactone/β-Tricalcium Phosphate Composite Scaffolds With Advanced Pore Geometries Promote Human Mesenchymal Stromal Cells' Osteogenic Differentiation," *Tissue Engineering—Part A* 31, no. 1–2 (2025): 13–28, https://doi.org/10.1089/TEN.TEA.2024.0030;PAGE:STRING:ARTICLE/CHAPTER.

61. F. Iberite, M. Piazzoni, D. Guarnera, et al., "Soft Perfusable Device to Culture Skeletal Muscle 3D Constructs in Air," *ACS Applied Bio Materials* 6, no. 7 (2023): 2712–2724, https://doi.org/10.1021/ACSABM.3C00215.

62. Y. Ren, J. A. Stobbs, D. J. Lee, D. Li, C. Karunakaran, and Y. Ai, "Utilizing Synchrotron-Based X-ray Micro-Computed Tomography to Visualize the Microscopic Structure of Starch Hydrogels In Situ," *Biomacromolecules* 25, no. 6 (2024): 3302–3311, https://doi.org/10.1021/ACS.BIOMAC.3C01438/SUPPL_FILE/BM3C01438_SI_008.MPG.

63. A. Khimchenko, C. Bikis, A. Pacureanu, et al., "Hard X-Ray Nanoholotomography: Large-Scale, Label-Free, 3D Neuroimaging Beyond Optical Limit," *Advanced Science* 5, no. 6 (2018): 1700694, https://doi.org/10.1002/ADVS.201700694;PAGE:STRING:ARTICLE/CHAPTER.

64. F. Cadamuro, L. Marongiu, M. Marino, et al., "3D Bioprinted Colorectal Cancer Models Based On Hyaluronic Acid And Signalling Glycans," *Carbohydrate Polymers* 302 (2023): 120395, https://doi.org/10.1016/J.CARBPOL.2022.120395.

65. M. Bracchi, F. Nicotra, and L. Russo, "3D Bioprintable Hydrogels Via Enzymatic Crosslinking Of Hyaluronic Acid And Phenol-Functionalized Gelatin To Mimic Extracellular (ECM) Network," *Carbohydrate Polymer Technologies and Applications* 11 (2025): 100928, https://doi.org/10.1016/J.CARPTA.2025.100928.

66. G. Cattoretti, F. M. Bosisio, L. Marcelis, and M. M. Bolognesi, "Multiple Iteractive Labeling by Antibody Neodeposition (MILAN)," *Protocol Exchange* (2019), https://dx.doi.org/10.21203/rs.2.1646/v5.

67. M. M. Bolognesi, M. Manzoni, C. R. Scalia, et al., "Multiplex Staining by Sequential Immunostaining and Antibody Removal on Routine Tissue Sections," *Journal of Histochemistry & Cytochemistry* 65, no. 8 (2017): 431–444, https://doi.org/10.1369/0022155417719419; CTYPE:STRING:JOURNAL.

68. R. Mokso, P. Cloetens, E. Maire, W. Ludwig, and J.-Y. Buffiere, "Nanoscale Zoom Tomography With Hard X Rays Using Kirkpatrick-Baez Optics," *Applied Physics Letters* 90 (2007): 144104, https://doi.org/10.1063/1.2719653.

69. D. Paganin, S. C. Mayo, T. E. Gureyev, P. R. Miller, and S. W. Wilkins, "Simultaneous Phase And Amplitude Extraction From A Single Defocused Image Of A Homogeneous Object," *Journal of Microscopy* 206, no. 1 (2002): 33–40, https://doi.org/10.1046/J.1365-2818.2002.01010.X.

70. P. Cloetens, W. Ludwig, J. Baruchel, et al., "Holotomography: Quantitative Phase Tomography With Micrometer Resolution Using Hard Synchrotron Radiation X Rays," *Applied Physics Letters* 75 (1999): 2912–2914, https://doi.org/10.1063/1.125225.

71. C. Olivier, M. Langer, B. Yu, et al., "Evaluation Of Phase Retrieval Approaches In Magnified X-Ray Phase Nano Computerized Tomography Applied To Bone Tissue," *Optics Express* 26, no. 9 (2018): 11110–11124, https://doi.org/10.1364/OE.26.011110.

72. B. Münch, P. Trtik, F. Marone, and M. Stampanoni, "Stripe And Ring Artifact Removal With Combined Wavelet — Fourier Filtering," *Optics Express* 17, no. 10 (2009): 8567–8591, https://doi.org/10.1364/OE.17.008567.

73. C. Tomasi and R. Manduchi, "Bilateral Filtering For Gray And Color Images," in Sixth International Conference on Computer Vision (IEEE, 1998), 839–846, https://doi.org/10.1109/ICCV.1998.710815.

74. SciCat Project, A meta data catalog and research data management system, https://github.com/scicatproject.

Supporting Information

Additional supporting information can be found online in the Supporting Information section.

Supporting File: adfm77772-sup-0001-SuppMat.docx.